JGR Space Physics

RESEARCH ARTICLE
10.1029/2019JA027200

Key Points:
- Seismically generated AGW dynamics from ground to exobase are simulated based on realistic spatial and temporal surface displacements
- Simulation results of near-epicentral ionospheric responses to AGWs are consistent with observations in amplitudes, periods, and speeds
- Results identify challenges and opportunities for faulting mechanism characterization based on ionospheric observations

Supporting Information:
- Supporting Information S1
- Movie S1
- Movie S2
- Movie S3

Correspondence to:
P. A. Inchin,
inchinp@my.erau.edu

Citation:
Inchin, P. A., Snively, J. B., Zettergren, M. D., Komjathy, A., Verkhoglyadova, O. P., & Tulasi Ram, S. (2020). Modeling of ionospheric responses to atmospheric acoustic and gravity waves driven by the 2015 Nepal M_w7.8 Gorkha earthquake. *Journal of Geophysical Research: Space Physics*, *125*, e2019JA027200. https://doi.org/10.1029/2019JA027200

Received 25 JUL 2019
Accepted 11 DEC 2019
Accepted article online 3 FEB 2020

Modeling of Ionospheric Responses to Atmospheric Acoustic and Gravity Waves Driven by the 2015 Nepal M_w7.8 Gorkha Earthquake

P. A. Inchin[1], J. B. Snively[1], M. D. Zettergren[1], A. Komjathy[2], O. P. Verkhoglyadova[2], and S. Tulasi Ram[3]

[1]Center for Space and Atmospheric Research and Physical Sciences Department, Embry-Riddle Aeronautical University, Daytona Beach, FL, USA, [2]Jet Propulsion Laboratory, California Institute of Technology, Pasadena, CA, USA, [3]Indian Institute of Geomagnetism, Navi Mumbai, India

Abstract Near- and far-field ionospheric responses to atmospheric acoustic and gravity waves (AGWs) generated by surface displacements during the 2015 Nepal M_w7.8 Gorkha earthquake are simulated. Realistic surface displacements driven by the earthquake are calculated in three-dimensional forward seismic waves propagation simulation, based on kinematic slip model. They are used to excite AGWs at ground level in the direct numerical simulation of three-dimensional nonlinear compressible Navier-Stokes equations with neutral atmosphere model, which is coupled with a two-dimensional nonlinear multifluid electrodynamic ionospheric model. The importance of incorporating earthquake rupture kinematics for the simulation of realistic coseismic ionospheric disturbances (CIDs) is demonstrated and the possibility of describing faulting mechanisms and surface deformations based on ionospheric observations is discussed in details. Simulation results at the near-epicentral region are comparable with total electron content (TEC) observations in periods (~3.3 and ~6-10 min for acoustic and gravity waves, respectively), propagation velocities (~0.92 km/s for acoustic waves) and amplitudes (up to ~2 TECu). Simulated far-field CIDs correspond to long-period (~4 mHz) Rayleigh waves (RWs), propagating with the same phase velocity of ~4 km/s. The characteristics of modeled RW-related ionospheric disturbances differ from previously-reported observations based on TEC data; possible reasons for these differences are discussed.

1. Introduction

Natural and anthropogenic hazards include sources of disturbances to solid (earthquakes and landslides), liquid (tsunamis), and gaseous (tornados, hurricanes, and volcanic eruptions) envelopes of the Earth. Being coupled with the atmosphere these disturbances may drive acoustic and gravity waves (for simplicity we will refer to both as AGWs together) propagating to the upper atmosphere (e.g., Hines, 1960). Due to exponential decrease of atmospheric density with altitude, at ionospheric heights AGWs can be strong enough to trigger detectable plasma perturbations, measurable using in situ or remote sensing instruments. One primary and readily available source of information on the ionospheric state is total electron content (TEC) measured from Global Navigational Satellite Systems (GNSS) signals (Parkinson et al., 1995). Detections of AGW-triggered plasma perturbations using TEC measurements have been reported on a consistent basis after strong earthquakes and tsunamis (Astafyeva et al., 2013; Ducic et al., 2003; Galvan et al., 2012; Occhipinti et al., 2013), severe tropospheric weather events (Azeem et al., 2015; Chou et al., 2017; Nishioka et al., 2013), and man-made activity such as rocket launches (Lin et al., 2017; Nakashima & Heki, 2014). Comprehensive reviews of ionospheric plasma perturbations driven by natural hazards and TEC measurements technique description can be found, for example, in Jin et al. (2015) and Komjathy et al. (2016). However, limitations of GNSS station coverage, as well as measurement techniques, in many cases preclude detailed analyses of ionospheric responses to AGWs. Limitations include the integrated nature of TEC along line-of-sight (LOS) between satellite and receiver, dependence of TEC amplitudes from mutual geometry of LOS and AGW wavefronts, registration of electron density fluctuations at altitudes starting from ionospheric F layer (~250 km) and usually low sampling rate. In situ diagnostics, airglow, and GNSS radio occultation measurements are potentially useful sources of information (Coïsson et al., 2015; Garcia et al., 2013; Pilger et al., 2013), but do not yet provide spatial and temporal resolution of data sufficient for comprehensive

investigation of earthquake-atmosphere-ionosphere coupling processes. Numerical simulations are an important and necessary step for deeper understanding of ionospheric responses to atmospheric acoustic and gravity waves, as well as understanding how we can observe them.

Modeling efforts have been made for the simulation of AGW propagation and driving of ionospheric disturbances after inland and undersea earthquakes, revealing important features that support theoretical results. Among them, Matsumura et al. (2011) reported simulation results of plasma perturbations driven by AGWs from impulsive upward surface motion with the use of a numerical model for the solution of Navier-Stokes equations for neutral atmosphere. Hickey et al. (2009) quantitatively described the AGW dynamics generated by a tsunami-like source using a linearized, steady-state Navier-Stokes equations model and derived TEC perturbations. Rolland et al. (2011) simulated coseismic ionospheric disturbances (CIDs) driven by acoustic waves (AWs) generated by Rayleigh waves (RWs) after the 2008 M_w7.9 Wenchuan and the 2003 M_w8.3 Tokachi-Oki earthquakes using Earth normal modes modeling and simplified neutral-plasma coupling approach. Simulation results of gravity waves driven by the 2004 M_w8.8 Sumatran and the 2011 M_w9.0 Tohoku-oki tsunamis in 3-D neutral-plasma coupled model (based on Boussinesq approximation without incorporation of thermoviscous dissipation) were published in Occhipinti et al. (2006, 2011). Recently, Meng et al. (2018) presented results of near-epicentral simulations with point representation of AGW source based on actual seismic data for the 2011 M_w9.0 Tohoku-oki and the 2015 M_w8.3 Illapel earthquakes. Zettergren and Snively (2015) presented modeling and analyses of ionospheric plasma density field responses to different time-dependent near-surface sources of AGWs. Zettergren et al. (2017) reported simulations of nonlinear AGWs effects, including plasma depletion "holes" (the decrease of absolute electron density that is persistent over multiple oscillations from the propagation of AWs and conducted by comparatively long-period recovering phase), after the 2011 M_w9.0 Tohoku-oki earthquake using an axisymmetric source based on initial ocean surface displacement data. For the same event Zettergren and Snively (2019) presented results of TEC and magnetic field fluctuations driven by the same AGW sources with a new 3-D multifluid-electrodynamic ionospheric model (GEMINI 3D).

In the majority of prior simulations of coseismic AGW propagation and plasma disturbances, ground-level sources of displacements are usually highly simplified (e.g., Zettergren et al., 2017). Assumptions based on maximum surface vertical velocities and the time and spatial scales of motion can serve as a good starting point, but cannot provide realistic source frequency response information which may markedly differ from earthquake to earthquake. This is particularly important for the simulation of near-epicentral acoustic wave propagation which include formation of shocks, thermoviscous dissipation, reflection/refraction, and ducted resonances. Point or axisymmetric (evenly distributed) sources do not incorporate the comprehensive surface deformation dynamics driven by earthquake faulting processes, as well as seismic waves propagation. These simplified sources are thus not always applicable for the simulation of near-field AGWs, especially for strong earthquakes (which usually trigger readily observable CIDs) when the faulting processes can take several minutes and be distributed on the domain of hundreds of kilometers. Such simplified sources also assume spatially frozen ground surface motion, whereas, in reality, the sources of AGWs include rupture propagation at supersonic speeds. Realistic representation of AGWs sources can improve spatial and temporal quality of simulation and fidelity to observations, and thus be helpful for deeper understanding of coupling processes. The use of stable, nonlinear, neutral atmosphere and ionosphere models, which resolve strong atmospheric disturbances correctly and applicably for simulation of short period acoustic and gravity waves (1–20 min), is also an important factor in successful reproduction of observed phenomena (Chum et al., 2016).

Earthquakes serve as a source of AGWs via their intense permanent surface displacements at focal area and (to a lesser extent) via transient surface displacements driven by the propagation of seismic waves to far distances. Inland strong earthquakes happen less frequently than undersea ones (simply because of location of subduction zones where strong thrust earthquakes of M 8–9 are expected). The presence of appropriate local distance data to quantify near-field displacement dynamics allows modeling of realistic fault mechanics (Yue et al., 2016) and, as a result, enables simulations of earthquake-atmosphere-ionosphere coupling with better accuracy. We have chosen the 2015 M_w7.8 Gorkha earthquake in Nepal, which has been broadly investigated, as a demonstrative modeling case of coupling processes, the results of which are presented in this article. Near- and far-field surface displacement dynamics, calculated in a forward seismic wave propagation simulation based on kinematic slip model representation of the earthquake (Yue et al., 2016), is incorporated into 3-D neutral atmosphere-2-D ionosphere models (Zettergren & Snively, 2013, 2015). Simulations

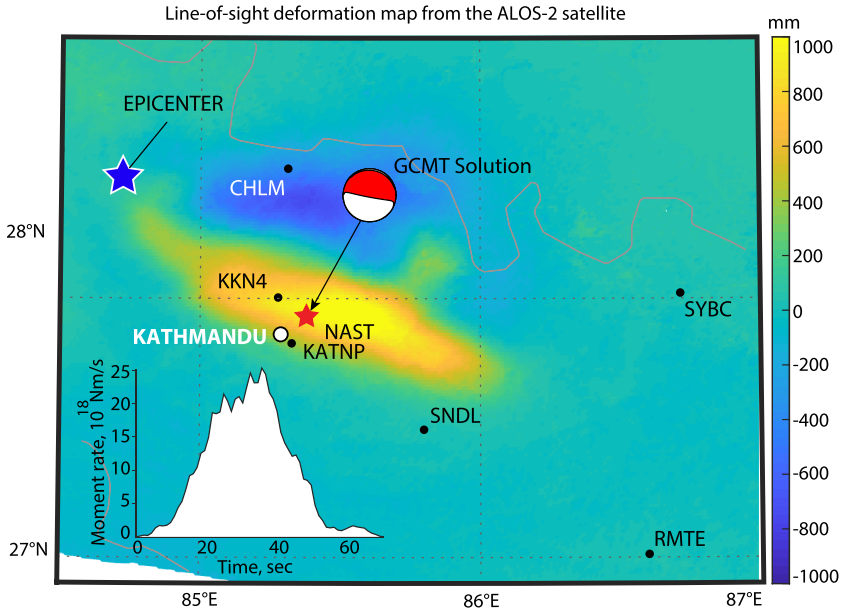

Figure 1. Line-of-sight vertical surface deformation data after the Nepal 2015 M_w7.8 Gorkha earthquake adapted from Lindsey et al. (2015). GCMT solution position, epicenter used in Yue et al. (2016) model, and the high-rate data GNSS stations positions used for seismic dynamic and CIDs analysis at near-field region are presented. The beach ball is based on the GCMT moment tensor. The moment rate function is adopted from Yue et al. (2016).

reveal amplitudes, periods, and velocities of near-field CIDs to compare with observations. We demonstrate the importance of incorporating near-field seismic wave dynamics for reproducing the observable spatial ionospheric nonuniformity of CIDs, as well testing the possibility to describe faulting mechanism of the earthquake based on ionospheric TEC data. Simulation results of far-field CIDs point to AWs driven by long period seismic waves as their sources. However, we find marked inconsistency of simulated far-field CIDs with RWs-related ionospheric disturbances, reported in some observational reports based on TEC data (e.g., Catherine et al., 2017; Reddy & Seemala, 2015), and we discuss these differences in detail.

The paper is structured by first providing information about the earthquake and generated surface displacements (section 2). Then, we review CID observations in literature, in addition to our own analyses of CIDs based on available TEC data for better understanding of observed phenomena (section 2.1). Section 3 describes the modeling approach used for simulations of AGWs and CIDs, including information about the models, their configurations and assumptions. In section 4 we present modeling results, first of the seismic waves propagation simulation, followed by the results of atmosphere-ionosphere simulations and analyses of AGWs and CIDs at near- and far-field from the epicenter. We discuss results and compare with observations. Finally, section 5 contains the discussion and conclusions.

2. Study Case Description

The Nepal Gorkha earthquake occurred on 25 April 2015 at 11:56:58 NST (06:11:58 UT) and was one of the most devastating in the last hundred years. It occurred at the Main Himalayan Thrust (Bilham et al., 2001), triggering around 4,000 landslides and more than 3,000 aftershocks within 45 days after the event (Adhikari et al., 2015; Kargel et al., 2016). According to Global Centroid Moment Tensor Catalog (GCMT) solution (Ekström et al., 2012), the earthquake generated a scalar moment of 8.39×10^{27} dyne-cm (M_w7.9); thrust (reverse fault) motion on the fault (Zhang et al., 2016) with 297°/6°/96° strike/dip/slip fault orientation parameters and epicenter at 27.91°N, 85.33°E and ~12 km depth (see Figure 1). Most finite-fault models showed in common that the rupture nucleated near the hypocenter and propagated to the southeast for 140–160 km with 50–60 km cross-strike extent and a velocity of 2.5–3.2 km/s (Fan & Shearer, 2015; Wei et al., 2018; Yue et al., 2016). It did not reach the surface and the earthquake ruptured only a deep part of the seismogenic zone (Kobayashi et al., 2015; Wang & Fialko, 2015). Reported slip distributions, based on different modeling techniques and data sets, vary markedly with maximum slips from 3.1 to 6.5 m (Zhang et al., 2016).

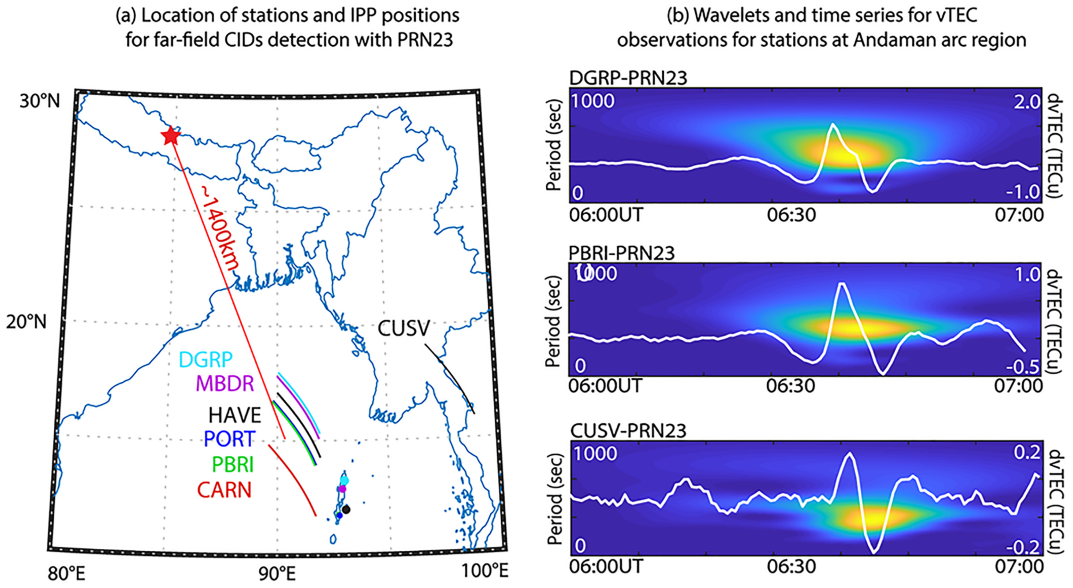

Figure 2. (a) Station locations map and their IPP positions with GPS PRN23 at the region where far-field ionospheric disturbances were mostly detected (on average ~1,400 km from the epicenter). (b) Wavelets and 10 min highpass filtered data for stations DGRP, PBRI, and CUSV showing ~6–10 min periods and 0.2–1.5 TECu amplitudes of observed vTEC perturbations.

Registered vertical surface displacements with a trough-to-peak amplitude up to 1.6 m (Lindsey et al., 2015) serve as a useful indicator that this earthquake may generate observable CIDs (Astafyeva et al., 2013). Vertical velocities found from strong motion accelerometers data and GNSS high-rate measurements were reported up to 64 cm/s (Takai et al., 2016). The region of uplift was larger and the amplitudes of uplift displacement were higher relative to subsidence zone (Kobayashi et al., 2015). According to low-frequency backprojection, three main stages of the rupture process can be defined: downdip rupture at the nucleation area for the first 20 s, then updip rupture which released most of the radiated energy from 20 to 40 s, and, finally, terminating stage with updip rupture (Fan & Shearer, 2015; Qin & Yao, 2017). This is fairly comparable with spatial distribution of vertical surface displacements based on ALOS-2 satellite data shown on Figure 1 (Lindsey et al., 2015).

2.1. Observed Coseismic Ionospheric Disturbances

Several comprehensive reports have been dedicated to the investigation of CIDs following this earthquake based on TEC data. Here we highlight some important observational aspects for the discussion of modeling results. Reports by Reddy and Seemala (2015), Tulasi Ram et al. (2017), Sunil et al. (2017), and Catherine et al. (2017) are based on similar data sets and are recommended for those interested in detailed observational studies connected with the earthquake.

One of the first reports, by Reddy and Seemala (2015), reported CIDs of maximum ~1.2 TECu (1TECu = 10^{16} el m^{-2}) propagating with 1.18 km/s (called "slow") and ~2.4 km/s ("fast") apparent phase velocities. The "slow" CIDs of ~4 mHz were connected with the propagation of AGWs triggered by near-field displacements, whereas the "fast" ones of ~2.7 mHz—with RW AWs. Reddy and Seemala compared detailed maps of RW fundamental group velocities from Acton et al. (2010) with apparent phase velocities of observable RW CIDs and pointed to their consistency in the Indo-Eurasian region. It should be noted that the map shown by Reddy and Seemala (2015) represents group velocities for 10 s period (fundamental mode) RWs. RW group velocity maps for 20–70 s fundamental modes were also provided by Acton et al. (2010) and may serve as a fairly good overview of RW group velocities in this region. From these maps, due to the highly dispersive nature of RWs, their group velocities at Indo-Eurasian region vary between ~1.8–4.2 km/s (generally, longer period RWs exhibit faster group/phase velocities). Reddy and Seemala (2015) also reported the separation of near-field CIDs and RW CIDs based on selected GNSS stations at Andaman arc region and nearby. We found that ionospheric pierce point (IPP) positions for those stations (DGRP, MBDR, HAVE, PBRI, PORT, CARN, and CUSV) with GPS satellites in the field of view after the earthquake (GPS PRN 03, 16, 23, 26, and 27) are, on average, at a distance of ~1,400–2,300 km from the epicenter (see Figure 2). Reddy and Seemala (2015)

reported the separation of near-field CIDs and RW CIDs at distance of 1,400–2,300 km from the epicenter. Though this distance varies depending on fault extension, mentioned by Reddy and Seemala (2015), distances seem to be much farther than reported previously, for example, 400–600 km reported by Astafyeva et al. (2009). Our modeling results suggest that these distances can be ~250 km (see section 4.2).

Tulasi Ram et al. (2017) reported TEC perturbations of 1.7 TECu (peak-to-peak), being stronger to east and south from epicenter. They also reported far-field CIDs, observed to the south from the epicenter, propagating with phase velocities ~1.73–2.39 km/s, but pointed to the inconsistency of the propagation velocities of these CIDs with RW group velocities calculated from seismometers data, which were reported as 3.4–3.7 km/s. It was concluded that there were no robust evidences of RW CIDs signatures in the available TEC data set.

Catherine et al. (2017) found near-epicentral CIDs propagating to the east with 0.98 km/s velocity, as well as ~0.65 km/s to the west from the epicenter with maximum amplitudes of 1.5 TECu to the east. Comparatively small velocities to the west were proposed to be a result of neutral winds impact and strong nonlinear effects. They reported far-field CIDs propagating with velocities of ~2.6 km/s and linked them with RWs, but it should be noted, that quite sparse set of TEC data were used and far-field CIDs were reported based on only one IPP track (see Figure 5a of Catherine et al., 2017).

Chen et al. (2017), Zhou et al. (2017), and Liu et al. (2017) also analyzed CIDs based on International GNSS Service and Crustal Movement Observation Network of China (CMONOC) data. Chen et al. (2017) found CIDs of maximum amplitude of 1.34 TECu propagating with 0.61 and 1.62 km/s and driven by near-field AGWs and RW AWs, respectively, at near-epicentral region, then RW CIDs with phase velocities of 2.35 km/s at 500–1,500 km distances and RW CIDs of 2.74 km/s at distances >1,500 km from epicenter. Liu et al. (2017) reported RW CIDs propagating with velocities 2.0–2.3 km/s. It is interesting to note, that analyzing the same set of data as in two previous reports, Zhou et al. (2017) failed to detect any RW CIDs. Difficulties with obtaining CMONOC GNSS stations data prohibit us from more detailed analysis of RW CIDs in that region.

All reports in common showed lower amplitudes of CIDs to north than to south and connected this with a dominant mobility of ions and electrons along magnetic field lines (Otsuka et al., 2006). Catherine et al. (2017) and Sunil et al. (2017) studied azimuthal asymmetry of near-field CIDs and its relation to east-southeast rupture propagation direction. First appearance of CIDs is shown between 8 and 11 min after the earthquake, which is consistent with time delay of propagation of AGWs to ionospheric heights. Sunil et al. (2017) and Tulasi Ram et al. (2017) investigated coseismic surface deformations and proposed that crust uplift at focal area led to initial high pressure phases of excited AWs (mostly to the south from strike direction), whereas crust subsidence resulted in the excitation of AWs with initial low-pressure phases (mostly to the north from strike direction). Uplift and subsidence zones can be discerned from Figure 1. The wide range of characteristics (amplitudes, velocities, and frequencies) of reported CIDs, as well as different explanation of observed phenomena, make this case to be of particular interest for modeling. The difficulty of the analysis of CIDs is partially related to quite sparse coverage of GNSS stations in the considered region.

The earthquake occurred during the local noon. The peak of the northern ionization crest of the equatorial ionization anomaly (EIA) was at the region of Nepal and north of India, resulting in enhancement of electron density up to 72–80 TECu in the proximity of the epicenter (see Figure 6). Geomagnetic conditions were relatively quiet with DST index of −15 nT, 126.2 $F10.7$ solar and ~2 Ap indexes.

For the investigation of CIDs, we used 0.2 and 30 s sampling rate GNSS TEC data obtained from UNAVCO archive and Indian Seismic and GNSS Network. Slant TEC (sTEC) and Vertical TEC (vTEC) were calculated using Jet Propulsion Laboratory software from raw satellite navigation system data in Receiver Independent Exchange Format. For the calculation of IPP coordinates, that represent the position of the intersection of satellite-receiver LOS and ionospheric shell layer (which approximates ionosphere as a infinitesimally thin spherical shell), we chose fixed height of ionosheric shell at 350 km.

Our analysis of near-field perturbation using vTEC data revealed first CIDs ~8–9 min after rupture nucleation and maximum amplitudes of ~1.4 TECu (see Figure 3). Azimuthal dependence of observable CIDs is presented; stronger CIDs were detected to the east (e.g., KKN4-PRN16, SYBC-PRN16, CHLM-PRN16, NAGP-PRN27, and LCK4-PRN27) from the epicenter and weaker (~0.1–0.2 TECu or nondetectable) to the northwest and west (LCK3-PRN16, GRHI-PRN16, and BMCL-PRN16). GPS satellites PRN 3 and 27 were useful for the detection of perturbation to the south, but at distances of ~300–600 km from epicenter with

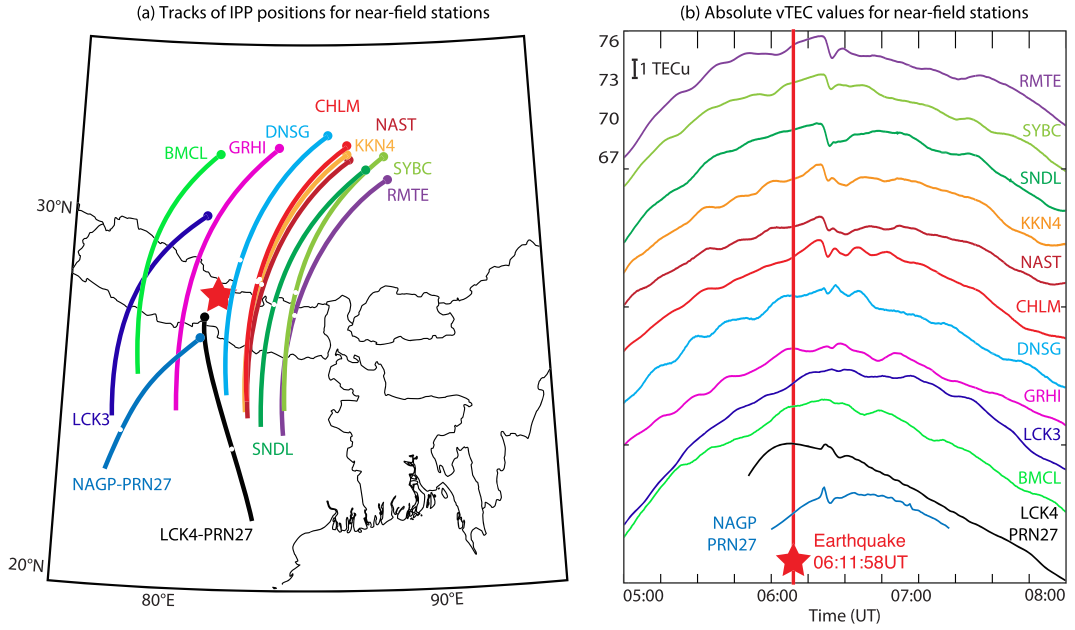

Figure 3. (a) Tracks of IPP positions for several high-rate GNSS stations near the epicenter with GPS satellite PRN16 (except LCK4-PRN27 and NAGP-PRN27 pairs, which are marked separately). Filled circle at the end of every IPP track presents final time tag and white circle along the track, time of CIDs detection. (b) Absolute vTEC time series are shifted one to another (not equally) for better visibility. For PRN16 the tracks are structured from east (top) to west (bottom). Real absolute values scale is valid only for station RMTE and presented for reference.

~30–50° LOS elevation angles. On Figure 3, two time series of TEC for pairs LCK4-PRN27 and NAGP-PRN27 are provided to show that sharp enhancements of vTEC were detected to the south. Clear evidence of ionospheric hole formation is presented for TEC observations with IPP positions close to the epicenter, for example, for pairs NAST-PRN16, SNDL-PRN16, KKN4-PRN16, and SYBC-PRN16. Electron density depleted to ~0.1–0.3 TECu after the passage of AGWs. It is fair to assume that the recovery phase took at least 30 min after the initial decrease in TEC driven by AGWs. The analysis of the recovery duration of electron depletion with TEC is complicated due to the fact that, after sharp decrease in TEC, the diurnal trend of electron density also started to decrease. In addition, the motion of IPP positions away from the focal area excluded the depletion region from observations, as, for example, for pair DNSG-PRN16.

On Figure 4 we present travel time diagrams for 10 min high-pass filtered vTEC data. The fault strike direction was approximately normal to local meridional direction (297°, GCMT solution), so we grouped vTEC measurements with IPP positions to the south and north only. For the investigation of near-field CIDs we used measurements with elevation angles higher than ~50° to exclude low-elevation angle data errors and to accurately calculate their propagation velocities. For the analysis of far-field CIDs, especially those in Andaman arc region, where elevation angles of measurements were ~25–40°, we present travel time diagrams for GPS satellites for which IPP positions were moving roughly to the north (PRN 16 and 26) and south (PRN 3 and 23) separately in order to exclude possible ambiguities in calculation of phase velocities.

Near-field CIDs propagated to north with velocities 0.76–0.96 km/s. Later in time, CIDs are detected propagating with velocities ~0.6 km/s, which may represent superposition of initial CIDs and those driven by reflected and ducted AGWs (see Figure 4a). For IPPs to the south, CIDs propagated with velocities 0.661.5 km/s at distances 0–1,400 km. Though not shown on plots, the periods of these CIDs are 3–8 min. There is a large gap in TEC measurements and detection of CIDs between ~800 and 1,400 km from the epicenter, which prohibits detailed analysis at these distances, leading to higher uncertainties in estimation of CID velocities. Further, as it was shown earlier, there is successful detection of ionospheric disturbances

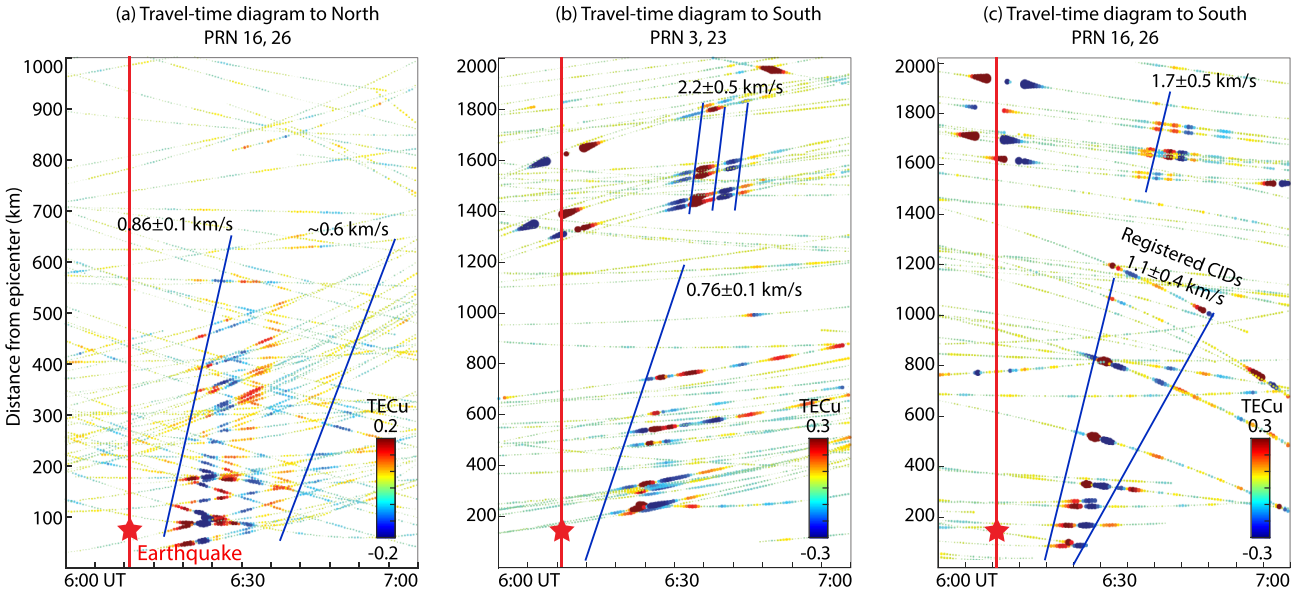

Figure 4. Travel time diagrams (distance of IPP positions from epicenter (ordinate) with time (abscissa)) for vTEC measurements with IPP positions to north from epicenter using (a) GPS PRN 16 and 26, (b) to south using GPS PRN 3 and 23 (satellites moving south), and (c) to south using GPS PRN 16 and 26 (satellites moving north). Detrended vTEC data (10 min high-pass filter) are presented as diamonds with different size depending on amplitude of CID. The data on plots are shown on an oversaturated scale for better visibility of weaker features.

(Figures 2, 4b, and 4c). These disturbances are detected at closest distance of ~1,400 km, with higher propagation velocities than those at near-field region. The same patterns can be seen on Figure 7b from Tulasi Ram et al. (2017), Figure 4,a from Reddy and Seemala (2015), Figure 5a from Catherine et al. (2017), and Figure 5d from Liu et al. (2017).

The use of such sparse data on a comparatively small time interval, as well as the low sampling rate data of 30 s, might introduce biases for determination of CIDs velocities. The same issue with determination of the velocities of CIDs was shown in Tulasi Ram et al. (2017), where phase velocities were reported as ~1.73–2.39 km/s. Also, it is difficult to address the belonging of some of the registered CIDs to particular phase fronts, as, for example, shown on Figures 4b and 4c at near field. Based on our analyses of data, we determined the velocities of far-field ionospheric disturbances to be ~1.7–2.7 and ~1.2–2.2 km/s for satellites moving to south (panel b) and north (panel c). We assume that the biases may be higher if velocities of IPP positions of vTEC measurements for low-elevation angles (up to ~0.3 km/s) are taken into account. We also found that far-field ionospheric disturbances exhibited comparatively long periods (6–10 min) and had high amplitudes - up to 1.5 TECu peak-to-peak (see Figure 2b).

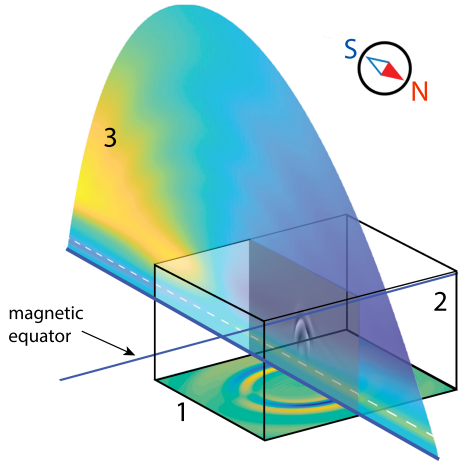

Figure 5. Earthquake-atmosphere-ionosphere model configurations. Surface vertical velocities driven by seismic wave dynamics (1) are used as a ground boundary condition at 3-D neutral atmosphere model MAGIC (2). The 2-D Ionospheric model GEMINI (3) accepts a meridional slice of data from MAGIC as an input (in velocities, densities, and temperatures) to simulate ionospheric responses over time.

Overall, using available TEC data sets, we found robust signatures of near-field CIDs. The azimuthal dependence of CIDs is presented with almost no detection of CIDs to west and northwest from the epicenter. We found that stations at Andaman arc region and nearby detected some ionospheric disturbances, but their characteristics do not provide clear conclusion that they are driven by RW AWs. Lack of observations does not allow us to unambiguously conclude that RW CIDs were registered

Table 1
Kinematic Slip Model Parameters Based on Yue et al. (2016)

Parameter	Value
Hypocenter	28.1473°N, 84.7079°E, 10 km depth
Seismic moment	6.40×10^{21} Nm (M_w7.8)
Fault parameterization	6° uniform dip angle
Subfaults	18 × 9 along-strike and down-dip direction, 10 × 10 km each
Rupture velocity	3.2 km/s
Maximum slip	~6 m at ~100 km south-southeast from hypocenter

at all. We will continue this discussion in section 4.3, comparing observations with modeling results and reviewing possible causes of differences of mentioned characteristics.

3. Modeling Approach

For the modeling of realistic earthquake-atmosphere-ionosphere coupling processes, we combined three numerical models spanning from the Earth's surface to its atmosphere and ionosphere (see Figure 5). Vertical surface velocities from forward seismic waves propagation simulation using the SPECFEM3D-Globe model (Komatitsch & Tromp, 2002a; Komatitsch et al., 2009) are incorporated into the 3-D neutral atmosphere Model for Acoustic-Gravity wave Interactions and Coupling (MAGIC) (Snively, 2013) to simulate atmospheric dynamics, acoustic and gravity wave generation, propagation, and dissipation. Then, a meridional slice of interest from the MAGIC simulation is used as a time-dependent input to the 2-D Geospace Environment Model of Ion-Neutral Interactions (GEMINI) (Zettergren & Semeter, 2012) to simulate ionospheric responses that are driven by neutral forcing through neutral-ion drag and collisions, generated dynamo currents, and modifications to thermospheric densities. In the following subsections, the information about the models and their configurations are presented.

3.1. Seismic Wave Propagation Model Configuration

The reproduction of near-epicentral surface displacements, which are strongly affected by spatial structure, rupture behavior, and radiation patterns, requires 3-D simulation of seismic dynamics (Igel, 2017). We used the SPECFEM3D-Globe software, based on the spectral-element method, for forward simulations of three-dimensional global seismic wave propagation (Komatitsch & Tromp, 2002a). The software calculates seismic wave dynamics with high accuracy and allows incorporating Earth's ellipticity and rotation, topography, ocean effects, gravitational contributions, anisotropy, and attenuation into simulations. It should be noted that the incorporation of the ocean in the model is only for reproducing of load effects at the bottom (Komatitsch & Tromp, 2002b).

To simulate realistic near-field seismic wave dynamics, we used a kinematic slip model adapted from Yue et al. (2016), which is based on multitime window approach. The summary of model input parameters is presented in Table 1 and detailed information can be found in supplementary materials to Yue et al. (2016). Kinematic slip model parameters were converted to centroid-moment tensor solution formats applicable for the use in the SPECFEM3D-Globe model. We used Gaussian source-time function as discussed in Komatitsch and Tromp (2002a). Vertical surface displacements were calculated for the domain of 4,000 × 720 km along latitude and longitude, respectively, and GCMT epicenter coordinates as a center of the domain. For Earth's interior we used the three-dimensional anisotropic S362ANI (Kustowski et al., 2008) model with 3-D Crust2.0 (Bassin et al., 2000) crustal model. To eliminate numerical boundary reflection problems, a global simulation was performed. The time series of displacements in Seismic Analysis Code binary format were then differentiated with a standard second-order finite-difference scheme and resampled. The number of spectral elements along the surface of one side for every six chunks, which represent the cubed sphere, was set as 336 and. Since the accuracy of the results is determined by number of grid points per shortest wavelength, the simulation is accurate to a shortest period of ~12.95 s (77.2 mHz). The earthquake occurred in a highly varied topographical area that may provide additional effects on the propagation of short-period seismic waves. However, in our case, considering only comparatively long-period seismic wave propagation of the shortest period of 12 s, the effect of topography is considered to be negligible. In addition, source inversion algorithm for slip model used in Yue et al. (2016) does not include the

Table 2
Simulation Configurations Used

Simulation	Domain and resolution (lat., lon., alt.)	Investigation of
(1)	990 × 600 × 500 km, 1 × 2 × 0.25 km	near-field ionospheric responses
(2)	600 × 600 × 300 km, 1 × 1 × 0.25 km	spatial dynamics of AGWs
(3)	4,000 × 500 km, 0.2 km uniform	seismic wave-driven AGWs and CIDs

topography and, thus (as it is inconsistent with the inversion used) we found that its incorporation indeed provides worse agreement with observations.

3.2. Atmosphere-Ionosphere Coupled Model Setup

MAGIC solves compressible, nonlinear Navier-Stokes equations as described in Snively (2013) and Zettergren and Snively (2015), based on shock-capturing finite volume methods of Langseth and LeVeque (2000) and Bale et al. (2002) in a modified version of Clawpack 4.2 (Clawpack Development Team, 2002; LeVeque, 2002). MAGIC accounts for nonlinearity and dissipation effects which play a crucial role on the propagation of AGWs (e.g., Heale et al., 2014; Sabatini et al., 2016, 2019). In particular, the need to accurately resolve the nonlinear effects of AWs at the near-epicentral region, where the amplitudes of vertical fluid velocities of AWs reach ~300 m/s, is one of the main challenges in the current study. Preliminary discussion of our assumptions is provided in this section.

In this report, we present results of several simulations, domain sizes, and resolutions of which are presented in Table 2. Simulation (1) is intended to investigate AGW excitation, propagation, and dissipation at near-epicentral region, and its output is used as a source of neutral perturbations for the ionospheric model GEMINI; Simulation (2), with a numerical domain up to 300 km, is designed to investigate the development of AGW patterns at constant altitude of 250 km where the ion-neutral collisional moment transfer is dominant; Simulation (3), with an extended latitudinal domain, is used for the investigation of AW propagation (and ionospheric perturbations driven by them) from surface displacements driven by seismic waves at far field. After preliminary tests, we found that resolving waves up to the frequency of 0.08 Hz is appropriate for an accurate investigation of the AGW dynamics in upper atmosphere and ionospheric plasma responses. This configuration of simulations was chosen to mitigate computational expenses.

The main trigger for detectable plasma perturbations and for the generation of ion-acoustic waves in the considered study case is a dominant ion-neutral collisional transfer of momenta in the 200–400 km region; AWs in this region found to have largest vertical velocities and the plasma density is high enough so perturbations are easily observable. Thus, for Simulation (1), we applied a wave-absorbing ("sponge") layer at altitudes 470–500 km and set the kinematic viscosity and thermal conduction coefficients as constant over this altitude range. When solving Navier-Stokes equations with accurate explicit numerical schemes, large values of these coefficients at higher altitude require drastically decreased time steps in order to satisfy stability conditions; this leads to marked increase in computational cost. The assumption to stop increasing the coefficients at high altitudes and to instead damp waves frictionally where the effects of neutrals on plasma perturbations are comparatively small allows us to save considerable computational time but still obtain robust results. Based on simulation test results, we estimate possible error due to this assumption to be not higher than a few percent. Simulation (2), which is dedicated to study the spatial dependence of AGW patterns from surface dynamics, does not require coupling with the ionospheric model and can be run up to comparatively lower altitudes than Simulation (1) without any additional restrictions. Simulation (3) requires an axisymmetric source in order to eliminate discontinuities at the center ($r = 0$). However, being still interested in simulating AWs propagating at far fields within the axisymmetric model to preserve geometrical spreading, we smoothly suppressed surface perturbations near the epicenter (±300 km to north and south). By doing so, we eliminated the near-field perturbations, which we investigate through Simulations (1) and (2) and are able to simulate AWs propagation at far field in 2-D up to the altitude of 500 km in polar coordinates with high spatial resolution and without additional restrictions. As the waves never intersect, the requirement for even symmetry is relaxed.

At the top and sides of the MAGIC numerical domain, we set boundary conditions that allow waves to pass freely through boundaries without reflection. As a bottom boundary condition, vertical surface velocities

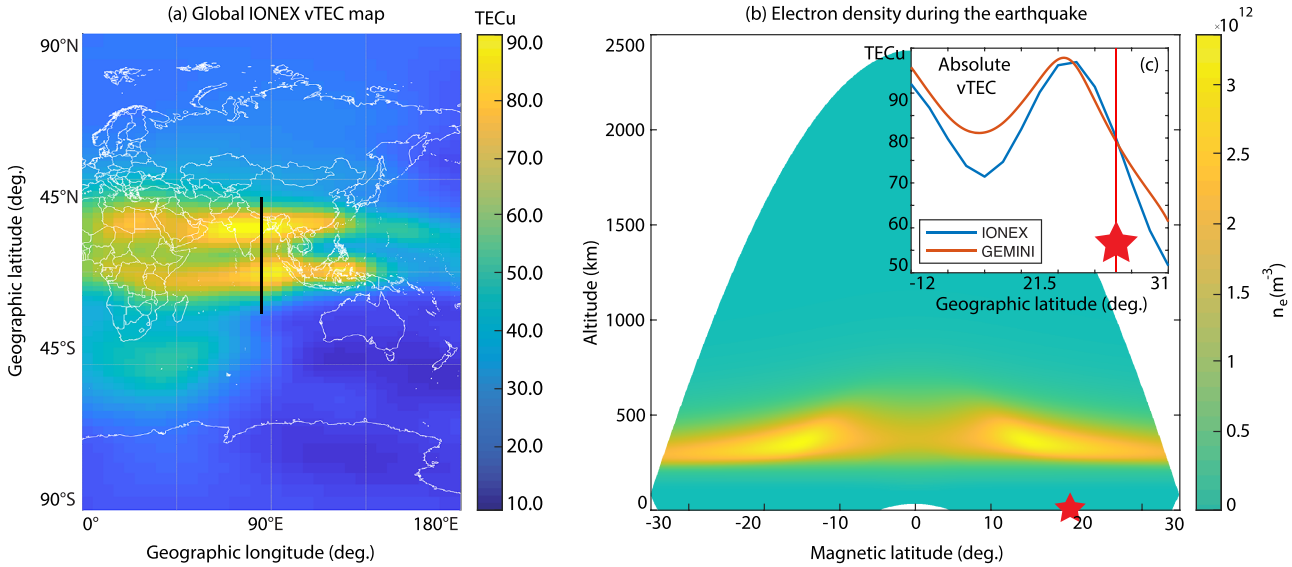

Figure 6. (a) Global vTEC map (IONEX) calculated by JPL at time of earthquake (12:00:00 LT). The ionospheric region above Indian peninsula and partially Nepal is affected by EIA. (b) The background electron densities map from GEMINI meridional slice (shown on panel a as black line) used in Simulation (1). (c) Comparison of absolute vTEC between IONEX and GEMINI.

calculated in SPECFEM3D-Globe are applied until surface velocities become negligible. After RWs leave the domain, an impermeability condition is set at the bottom boundary to resolve AGW reflections.

The GEMINI model solves the conservation equations (mass, momentum, and energy) for each major ionospheric species ($s = O^+, NO^+, N_2^+, O_2^+, N^+, H^+$) with an electrostatic description of dynamo currents based on the five-moment approximation (Schunk & Nagy, 2009; Zettergren & Semeter, 2012; Zettergren & Snively, 2019). A tilted dipole coordinate system is used as a generalized orthogonal coordinate system (Huba et al., 2000). Densities of O, N_2, O_2, vertical and meridional velocities, and temperature perturbation data are sent from MAGIC to GEMINI time dependently to simulate ionospheric responses based on chemistry, collisions, drag, and production of electric fields by dynamo effects. For the analysis of CIDs in this report we used meridional slice at 85.35°E, which is in proximity of the GCMT solution epicenter (see Figure 1). Numerical boundaries for the calculation of electric potential were set as "grounded" (zero for all points at the boundaries). The MAGIC domain data are encapsulated into the overlapping GEMINI domain; the densities of neutrals at 500 km (top MAGIC boundary) are negligible and thus there are no discontinuities in parameters between the models at high altitudes.

The earthquake happened at local noon and in the proximity of the EIA crest region that is important to resolve in the simulation. The EIA markedly affects the resulting electron density perturbations (through the simulation with and without EIA, the results of which are not shown here, we found the difference of 0.6 TECu peak-to-peak in maximum perturbations). We implemented in GEMINI the same approach to model the EIA as described in Huba et al. (2000). A balanced ionospheric state was achieved by running an additional GEMINI simulation for 24 hr prior to the event to ensure a set of state parameters that are a good representation of the ionosphere. Figure 6 shows the results of electron density for GEMINI, as well as comparison of absolute vTEC values for latitudes of earthquake epicenter (27.91°N) calculated in GEMINI and obtained from JPL IONEX map for 12:00:00 LT. We found that ground-based TEC observations are the most appropriate source of data for the comparison of electron density in the region of interest during the event, though providing only integrated values. We obtained fairly good agreement between vertically integrated electron densities from the simulation and vTEC data at near-epicentral region, but differences can be seen at magnetic equator (Figure 6c). Though our neutral atmosphere simulations domains do not reach the magnetic equator region, it should be noted that IONEX maps represent interpolated vTEC data from a sparse network of stations with 2.5° by 5° resolution (in latitude and longitude directions, respectively) grid, as well sparse in time domain, and cannot serve as a robust reference for comparison. We also compared vertically integrated electron density profiles from our simulation with absolute vTEC values calculated for satellite station pairs at near-field region (~72–80 TECu) and found fairly good agreement.

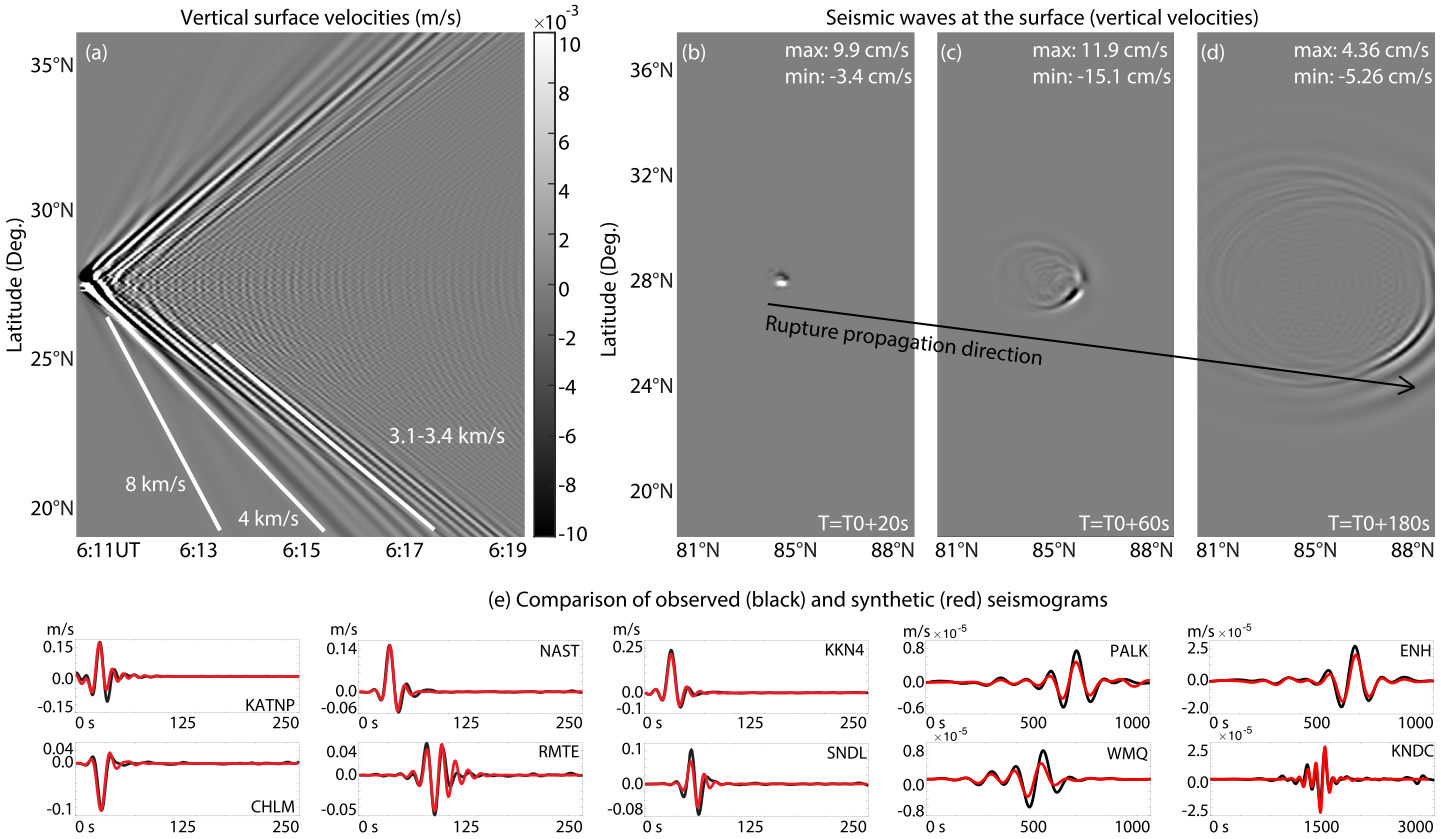

Figure 7. (a) Time-latitude diagram of surface vertical velocities along 85.35° longitude. The color scale is saturated to depict the propagation of surface waves at far distances. (b–d) The development of seismic waves at surface for 20, 60, and 180 s after rupture nucleation. (e) Observed (black) and predicted (red) seismograms, where near-field stations (KATNP, NAST, KKN4, CHLM, RMTE, and SNDL) waveforms are filtered with 0.07 Hz Butterworth low-pass filter; for far-field broadband seismometers (PALK, WMQ, ENH, and KNDC), the instrumental response was removed and seismograms were filtered with 0.003–0.01 Hz band-pass filter.

The 1-D vertical profiles of the ambient neutral atmospheric state for MAGIC and GEMINI models were calculated using the empirical model NRLMSISE00 (Picone et al., 2002). One-dimensional vertical profiles of both meridional and zonal winds were determined using HWM-14 model (Drob et al., 2015) and incorporated into MAGIC simulations and then encapsulated into GEMINI simulation as a part of meridional fluid velocity. These profiles remain stationary, assuming that their change is negligible over the considered time frame and chosen spatial domain.

4. Simulation Results and Discussion

4.1. Surface Seismic Waves Dynamic Simulation Results

To validate simulation results we compared synthetic seismograms with processed and reviewed data for strong motion accelerometer KATNP maintained by United States Geological Survey, high-rate continuous GPS (cGPS) data, which are applicable for studies of near-field faulting dynamics (Crowell et al., 2012) and far-field GSN broadband seismometers data from IRIS DMC archives. Data from cGPS stations (5 Hz), four of which are located at rupture zone (CHLM, KKN4, NAST, and SNDL), were obtained through the UNAVCO service. Receiver Independent Exchange Format data were processed using Precise Point Positioning Kinematic service provided by Natural REsources Canada to calculate surface displacements.

Stations KATNP and NAST are placed in the Kathmandu basin, which is located mostly on sediment between igneous rocks leading the whole basin to serve as a resonator for seismic waves (Fujii & Sakai, 2002) with observable 4–5 s period shaking (Galetzka et al., 2015); this is problematic to resolve in our simulations. However, we do not simulate surface dynamics up to such high frequencies, because their contribution to CIDs is fairly negligible. For comparison of observation and synthetic data we included stations in Kathmandu basin too.

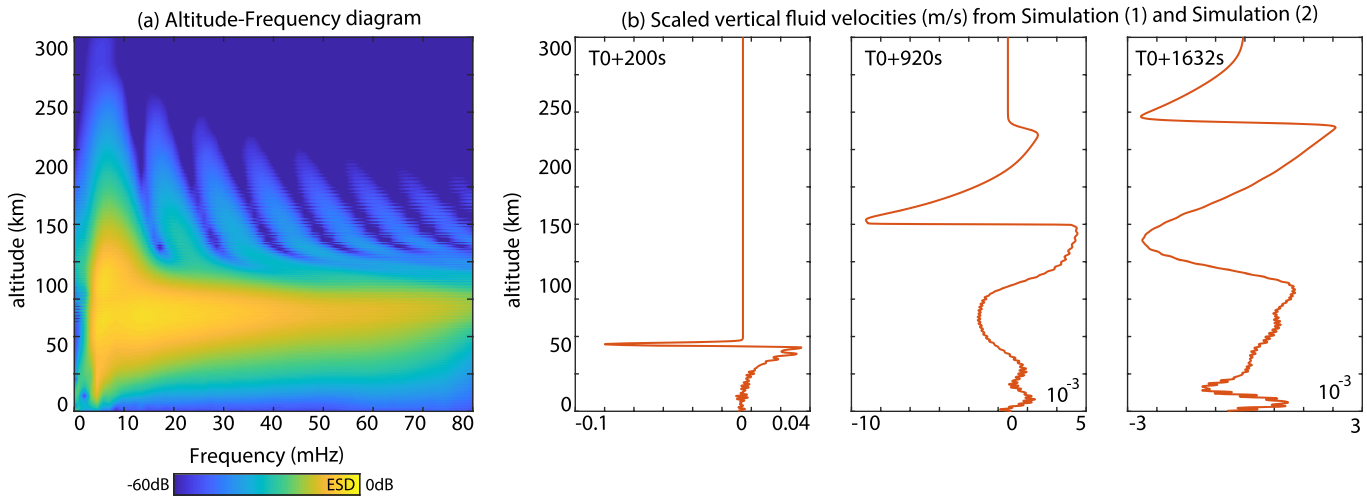

Figure 8. (a) Energy spectral density diagram of frequency-altitude profile for the point 10 km to the north from GCMT epicenter. (b) Scaled vertical fluid velocities for three time epochs.

Reasonable agreement between simulation and observations is found (see Figure 7). Comparison of RW phase velocities from simulation with regional maps of RW group velocities from Acton et al. (2010) and Ritzwoller and Levshin (1998) revealed their consistency for Indo-Eurasian region and Indian peninsula. Results also show that the simulation preserves the direction of rupture propagation to east-southeast from hypocenter. The main energy lobe of surface waves is directed to southeast, but the directivity is dominant for periods <80 s. For periods >100 s, the directivity effect is fairly small. This is in agreement with Duputel et al.'s (2016) comparison of observed and predicted seismograms based on CMT solution. For long-period RWs, the directivity played small role with only slightly higher amplitudes to the southeast. Thus, the comparison of simulation results with observations showed that such surface dynamic can be used as a realistic source of AGWs generated by the earthquake. Some inaccuracies can be connected with choices of different Earth models for source inversion in the kinematic slip model and that used in SPECFEM3D-Globe and topography, as well as source representation.

4.2. Atmosphere-Ionosphere Response Simulation Results

The coupling of surface displacements with the atmosphere results in the generation of AGWs, which propagate with velocities and amplitudes that depend on background state conditions (Bergmann, 1946; Mikhailov & Martynov, 2017). They can reach considerably high amplitudes in thermosphere; nonlinear effects of AW propagation in the near-epicentral region leads to the formation of shock waves. Figure 8a represents the energy spectral density of the scaled vertical velocities on an altitude-frequency diagram for the location 10 km to the north from the epicenter (GCMT) from Simulation (1). Scaled instantaneous vertical fluid velocity profiles for three time epochs are shown as well on Figure 8b. The generation of AW high frequency spectrum between the ground and mesopause is a consequence of the formation of shock waves (Sabatini et al., 2016). At higher altitudes, thermoviscous dissipation leads to attenuation of high-frequency AWs, along with shifting the AW spectrum to low frequencies due to the lengthening of nonlinear AWs. High-frequency content of AWs is markedly attenuated by these damping mechanisms at thermospheric heights corresponding to the ionospheric *F* layer and higher.

A series of snapshots of scaled pressure perturbations $p'/\sqrt{\rho/\rho(0)}$ (where p' = pressure perturbations, ρ = density, and 0 represents ground) from Simulation (1) of AGW propagation is presented on Figure 9. Positive (to the south from the epicenter) and negative (to the north) initial phases of leading AWs are clearly seen at altitudes lower than ~80 km (Figure 9a), because the strike direction was almost perpendicular to the local meridional direction, and plots represent meridional slices along the longitude of GCMT epicenter. This is approximately consistent with the map of surface displacements: uplift to the south and subsidence to the north from the strike direction. Refraction of AWs, both at stratospheric heights (~50 km) and at mesopause (~90–120 km), occurs. Increasing of amplitudes and steepening of AW fronts can be seen from the lower thermosphere, up to ~270 km.

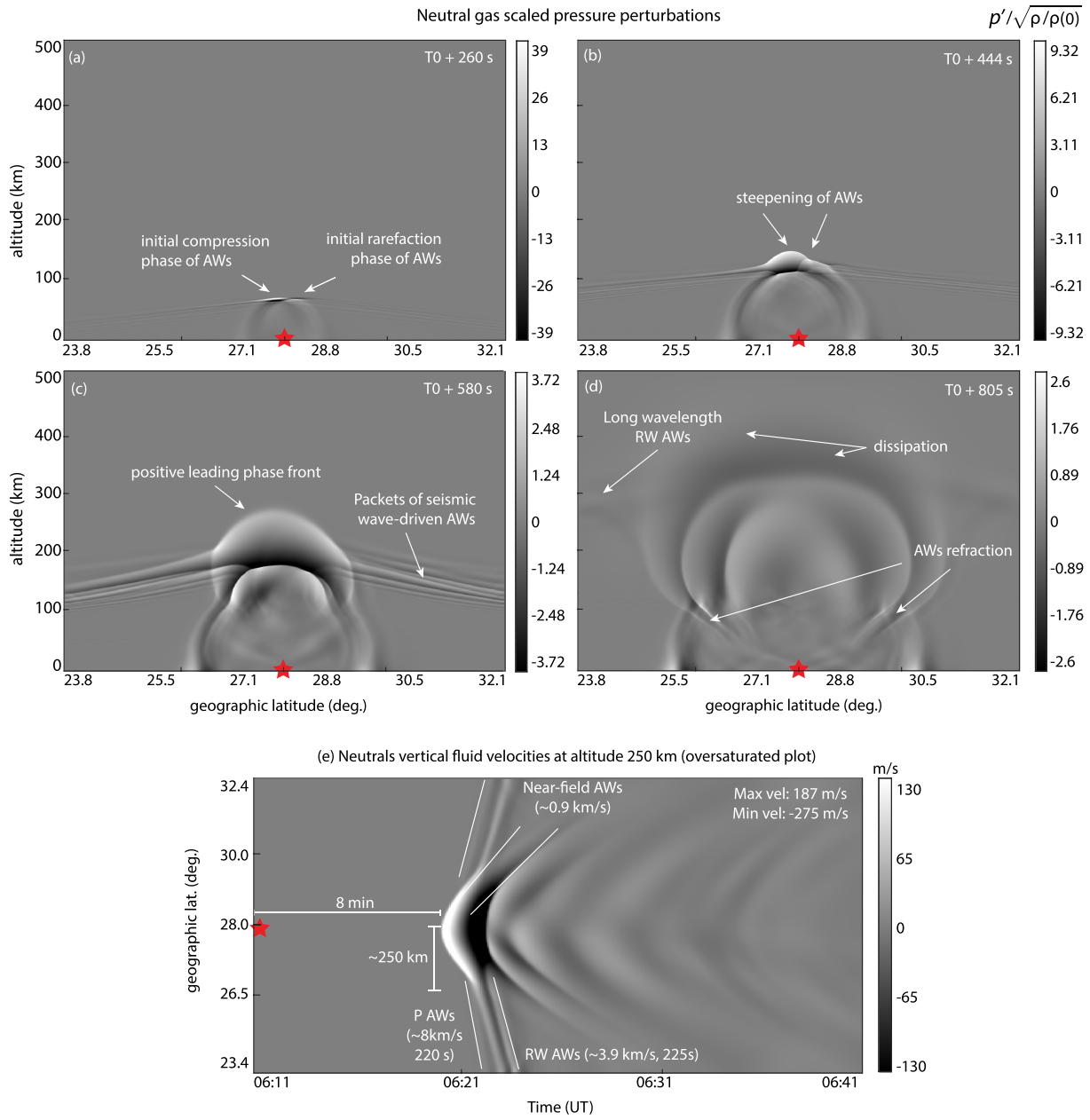

Figure 9. (a–d) Latitude-altitude slices of simulated scaled pressure perturbations for meridional slice along the GCMT epicenter based on Simulation (1). The epicenter latitude is indicated with a red star. Min/Max vertical velocities obtained from this simulation range from −280 to 187 m/s. (e) Oversaturated time-latitude diagram of vertical fluid velocities at altitude of 250 km for epicenter meridional slice.

Starting from the ionospheric *F* layer (~200 km and higher), leading AWs exhibit a uniform compressional phase front to the south and the north from the epicenter. Although the leading front is not fully meridionally symmetric, and AWs to north are lagged comparatively to AWs to the south (see Figures 9b and 9c), this difference is almost not detectable. This important result shows that the nonlinearity of strong near-epicentral shock AWs, their confluence and interference at near-field region, may change leading phase fronts during AW propagation to the thermosphere and even obscure phase information (Whitham, 1974). Also, strong AWs with initial compression phase, excited from uplift zone to the south, markedly obscure and overtake AWs excited from subsidence zone to the north. This raises concerns about the possibility to describe faulting mechanism and surface deformations based on ionospheric observations (particularly TEC) where waves become strongly nonlinear. Whereas for altitudes <100 km the uplift/subsidence pattern of excited AWs is still preserved, at thermospheric altitudes the nonlinearity of the propagating AWs, and their interference,

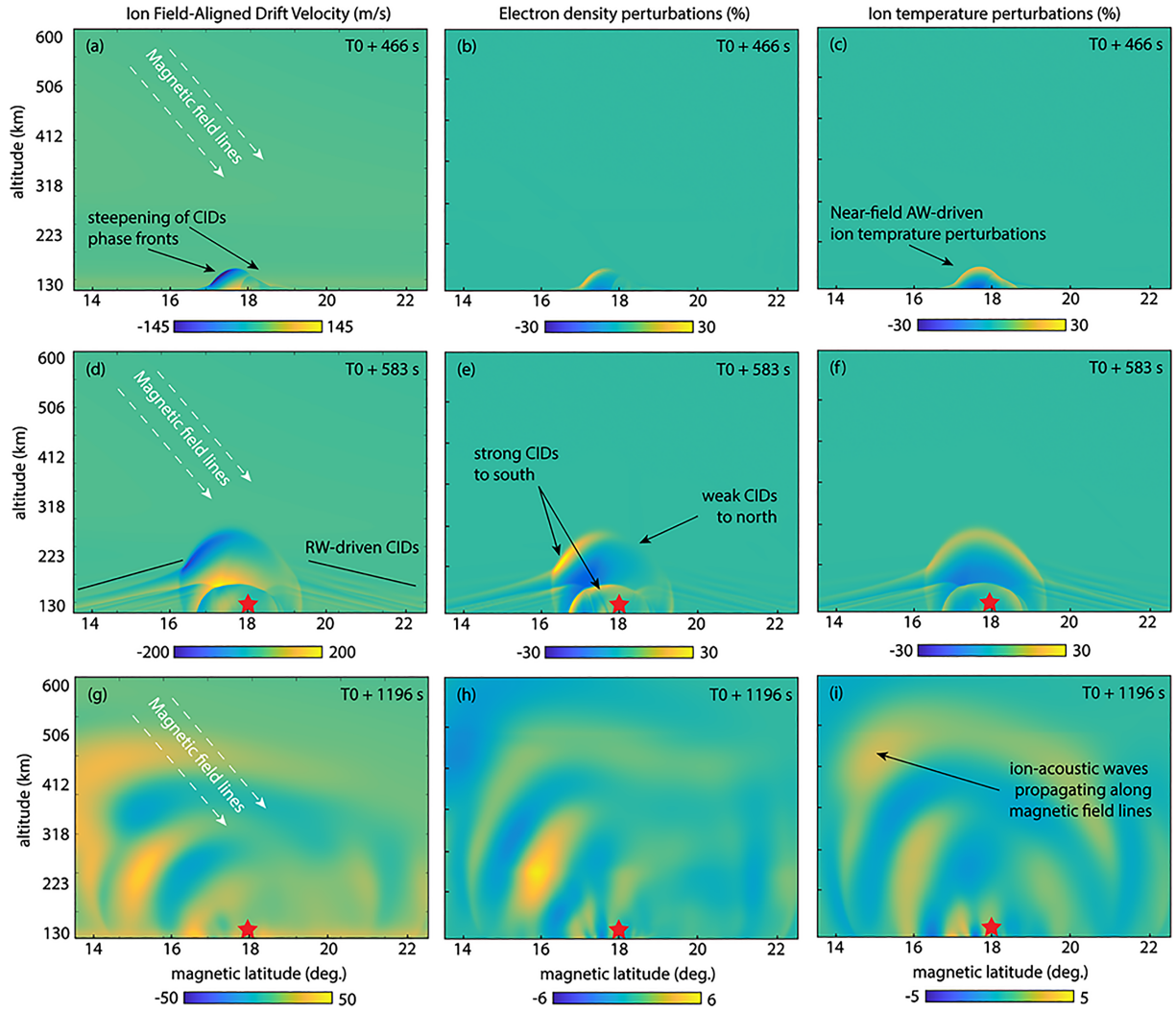

Figure 10. Ions field-aligned (positive downward) drift velocities (a, d, g), electron density perturbations (b, e, h), and ions temperature perturbations (c, f, i) for three time epochs from Simulation (1). Plasma motion at altitudes < ~300 km is driven by interaction with neutral species, and at higher altitudes, freely propagating ion-acoustic waves can be seen.

may completely change the initial phase structure of AW fronts, even forming uniform-looking shock fronts. This might be the reason why, for some cases, axisymmetric representation of sources for simulations of near-field disturbances provide quite good agreement with observations (e.g., Zettergren et al., 2017). However, as it is shown here, the dynamics of near-field AWs and the formation of leading phase fronts of AWs, may be much more complicated and lead to false conclusions about AWs propagation from surface to thermosphere. At the same time, simulation shows that AWs driven by seismic waves, at farther distances from epicenter, propagate in a fairly linear regime (due to low amplitudes), and their initial phases are preserved even at ionospheric altitudes.

Figure 9e represents time-latitude diagram of simulated neutral gas vertical fluid velocities at altitude 250 km along the longitude of the GCMT epicenter. Again, almost fully meridionally uniform AW fronts can be clearly seen, followed by strong AW rarefaction phases. Three distinct groups of AWs, propagating with velocities ~8, ~4, and ~0.9 km/s, are clearly seen. The fastest AWs are generated by surface displacements, that are consistent with phase velocities of *P* waves, as shown on Figure 7. They are of quite small amplitudes (~1–3 m/s peak-to-peak) and cannot be feasibly detected with TEC measurements, particularly due to the need of even lower LOS angle of measurements for their detection than for RW CIDs (see section 4.3). They may be observed with, for example, Doppler sounding systems (Chum et al., 2012). Second source of AWs are RWs and the correspondence between the phase velocities of comparatively long-period

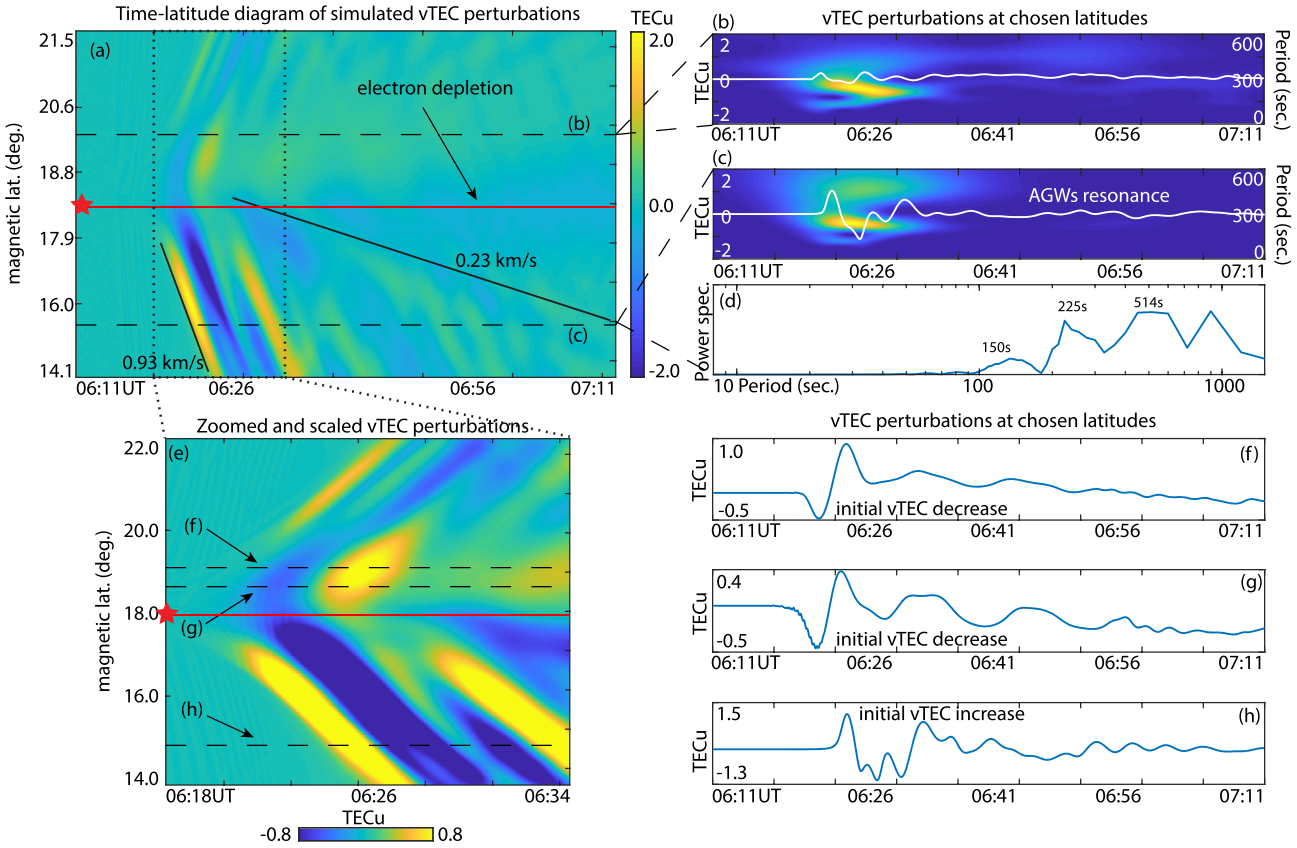

Figure 11. (a) Time-Latitude diagram of simulated vTEC perturbations; (b) and (c) time series of vTEC at chosen latitudes and their wavelet power spectra. (d) Fourier transform for plot (c). (e) Oversaturated time-latitude diagram of vTEC. (f-h) Time series of vTEC at chosen latitudes shown on panel e with black dashed lines.

RWs at the surface and of these AWs is preserved. Finally, the slowest perturbations of the highest amplitudes are driven by near-field AWs, propagating with phase velocity of ~0.8–9 km/s. Based on the analysis of CIDs after the Kurile 1994 M_w8.3 earthquake, Astafyeva et al. (2009) demonstrated that the perturbations driven by near-field AGWs and by RW AWs can be discerned at ~600–700 km from epicenter. This observation is supported by the fact that near-field seismic wave dynamics are usually very complex, especially for strong earthquakes where faulting process can develop on a region of hundreds of kilometers. It should be noted, that AW wavefronts and LOS geometry of TEC measurements may introduce additional biases here. Our results suggest, that the closest distance where RW AWs can be confidently discerned from near-field AGWs for the Nepal earthquake is ~250–400 km. This result differs markedly from that reported in Reddy and Seemala (2015) where separation of near-field and far-field CIDs was observed at distance of ~1,400–1,500 km.

Figure 10 depicts results of the GEMINI simulation of ionospheric plasma responses to the propagation of AGWs for three time epochs. Ion field-aligned drift velocity, plotted in these panels, is a density weighted value of six ion species velocities. Electron density and ion temperature perturbations are shown as the percentage change from the unperturbed state. Steep and nonlinear AWs at altitudes lower than 300–350 km (Figure 9), drive plasma responses by transport of charged particles confined predominantly along magnetic field lines toward the magnetic equator. As it was shown in Zettergren and Snively (2015), the plasma motion for altitudes lower than ~300–400 km is driven mostly by directly forced perturbations from the neutral gas. At altitudes higher than ~400 km, plasma velocities become larger in magnitude, due to coupling with nearly freely propagating ion-acoustic waves at higher phase speeds. The same pattern can be seen in our simulation. Latitudinal asymmetry of electron density perturbations is clearly seen on Figures 10b, 10e, and 10h. Ions in E and F ionospheric layers, due to the heat exchange with neutrals through the collisional interaction and plasma compression and rarefaction driven by AW propagation, exhibit similar pattern of

temperature perturbations as for neutral gas shown on Figures 9b and 9c. At higher altitudes, there are freely propagating ion-acoustic waves along magnetic field lines and almost no perturbations driven by AWs.

We calculated vTEC perturbations from the Simulation (1) for a meridional slice along the epicenter (Figures 11a and 11b). To do so, for every point on a grid, we integrated electron density along the radial direction, which corresponds to 90° elevation angle LOS. The time-latitude diagram shows important nuances of vTEC measurements for the detection of CIDs in the vicinity of the epicenter, where the plasma motion relative to LOS of vTEC is almost perpendicular (zenith). Right above the epicenter (18.1° magnetic latitude), only small electron density perturbations are represented (though perturbations can be clearly seen from time-latitude diagram of vertical fluid velocities on Figure 9e). The perturbations can be clearly distinguished in vTEC within the fidelity of our simulation at distances ~50–60 km from the epicenter. This results from several factors: (1) the directivity of rupture propagation that drove the strongest AGWs to southeast, (2) dominant plasma mobility along magnetic field lines, and (3) direction of LOS used (vertical integration of electron density for each point of the numerical domain). Figure 11a shows that initial enhancement of vTEC to the north from the epicenter is barely seen, whereas, to the south, vTEC enhancement is readily detectable. This is related to meridional plasma response asymmetry, discussed in previous paragraph. Following downward motion of plasma produces quite intense perturbation to north and to south (due to much stronger perturbations: 187 m/s at the leading compression AW phase, versus −281 m/s of the following rarefaction AW phase of vertical fluid velocities). The propagation velocities of CIDs, driven by near-field acoustic and gravity waves, are calculated as 0.92–0.95 and 0.21 km/s, with periods of 200–225 and 514–720 s, respectively. Observed phase velocities of 0.92–0.95 km/s of CIDs are fairly consistent with simulated near-field AGW phase velocities, shown on time-latitude diagram on Figure 9e. Maximum perturbations from presented vTEC latitude-time diagrams are found to be ~2 TECu.

Electron density depletion can be seen on Figure 11a, as a persistent decrease of electron density in the vicinity of the epicenter, which can indicate a nonlinear (semi-permanent) response to the propagation of AWs due to transport of plasma that may also lead to a higher rate of recombination (Zettergren et al., 2017). Its magnitude is 0.15–0.17 TECu and comparable with magnitudes presented in past observational reports (Masashi et al., 2015; Tulasi Ram et al., 2017) and with results of our analysis in section 2. The magnitude is small, in comparison, for example, with the 2011 Tohoku M_w9.1 earthquake, where AGWs drove a TEC depletion of 4–5 TECu (Saito et al., 2011; Zettergren & Snively, 2019; Zettergren et al., 2017). We assume that this is due to the much smaller amplitudes of AGWs for the Nepal earthquake. Tulasi Ram et al. (2017) reported the duration of the ionospheric hole's recovery phase as approximately 4–5 min, but pointed out the difficulty for the estimation, due to the superposition of different CIDs. This difficulty might also be connected with the motion of IPP position of TEC measurements within the spatially constrained region of the ionospheric hole (in simulation it is of only ~200 km latitudinal size), as well as with diurnal electron density variations. Simulation results suggest that the ionospheric hole may exist for a long duration, even 1 hr after the earthquake. The acoustic resonances, generated by trapping of AWs between lower thermosphere and tropopause/surface, can also be seen from Figures 11b and 11c at times ~06:50 UT, indicating the arrival of the second AWs packet "burst" with similar periods as the first one (~220–225 s).

As shown in Figure 3, a sharp decrease of electron density was registered in TEC for satellite-station pairs with IPP to the north from the epicenter, that was linked with AWs with initial rarefaction phases excited at crust subsidence (Sunil et al., 2017). Simulated vTEC time-latitude diagram, two vTEC time series, slightly to the north from epicenter, and one vTEC time series far to the south, are shown on Figures 11e–11h, respectively. The replication of exact TEC measurements without full 3-D ionosphere simulation is not possible. However, the provided time series are comparable with TEC observations for pairs DNSG-PRN16 and LCK4-PRN27, with IPP positions to north and south from epicenter, respectively. Figures 11f–11h show that in the proximity of the epicenter to north, only the depletion phase of vTEC may be registered initially, which could lead to false interpretation of these dynamics to be driven by AWs with initial rarefaction phases, excited at subsidence zone. Observed vTEC enhancement to the south from the epicenter can be seen in our simulation results shown on Figure 11h.

This simple demonstration, based on simulated vTEC, shows that initial decrease in TEC perturbations may not necessarily be connected with AWs excited with initial rarefaction phase from subsidence of the crust. It should be noted that usually low sampling rate and LOS of TEC measurement geometry and direction of the CIDs' fronts might also lead to misinterpretation of the sequence of phase fronts for observed

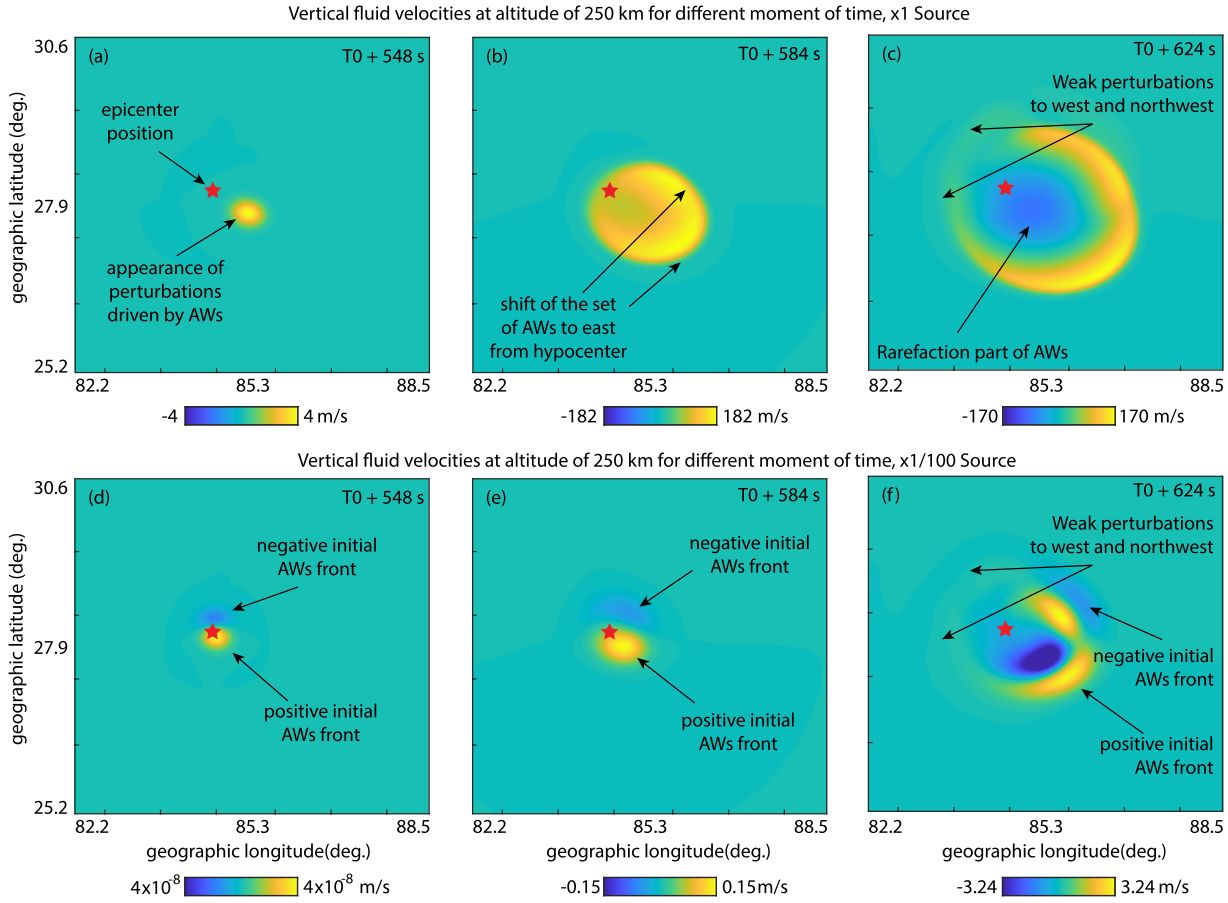

Figure 12. Panels (a,b,c) show nonlinear AW dynamics at near-epicentral region at fixed altitude. The dislocation of AWs from earthquake hypocenter to east is clearly seen, where there are almost no AWs propagating to west and northwest. Panels (d,e,f) show AW dynamics for same time epochs and 1/100 magnitude of the source. In this linear regime, phase information of leading AWs is preserved.

CIDs driven by different AWs. In addition, the spatial and temporal complexity of the source can complicate data analyses. Meng et al. (2018) addressed this problem based on simulations of the 2011 M_w9.0 Tohoku-oki and the 2015 M_w8.3 Illapel earthquakes. They found that an axisymmetric AW source driving global ionosphere-thermosphere model (GITM), without any direction preference, provides quite different latitudinal patterns of TEC perturbations. Zettergren and Snively (2019) investigated this latitudinal asymmetry of driven CIDs with the use of an axisymmetric source of AGWs and concluded that dominant motion of plasma along magnetic field lines markedly affects the spatial structure of CIDs. The description of faulting mechanism and surface deformations based on TEC measurements still requires additional investigations particularly through comprehensive modeling studies.

The last aspect we would like to address is the longitudinal dependence of AW and CID dynamics from surface displacement dynamics. As it was shown in section 2.1, during the earthquake TEC perturbations were observed mostly to the south, southeast, and northeast from the epicenter, whereas to the west and northwest there were almost no observable CIDs. The same spatial pattern was obtained through Simulation (2), see Figures 12a–12c. The radiated AWs shifted approximately from the epicenter position to the east, southeast, and northeast. The most intense AWs (Figure 12c) were excited to the southeast. This is consistent with the fact that maximum energy release happened at ~100 km from the epicenter position, while the rupture propagated to southeast, close to the longitude of GCMT epicenter. At the same time, there were almost no excited AGWs to the west but especially not to the northwest. This points to the advantage of the incorporation of finite-fault models for accurate representation of excited AWs at near-field region. Point or axisymmetric sources, frozen at one location would not be able to reproduce this important feature; in our case, the source of AWs is moving with propagation of rupture to southeast at supersonic speed of 3.2 km/s, and closely replicated surface displacement dynamics in time and space. The dependence of AW initial

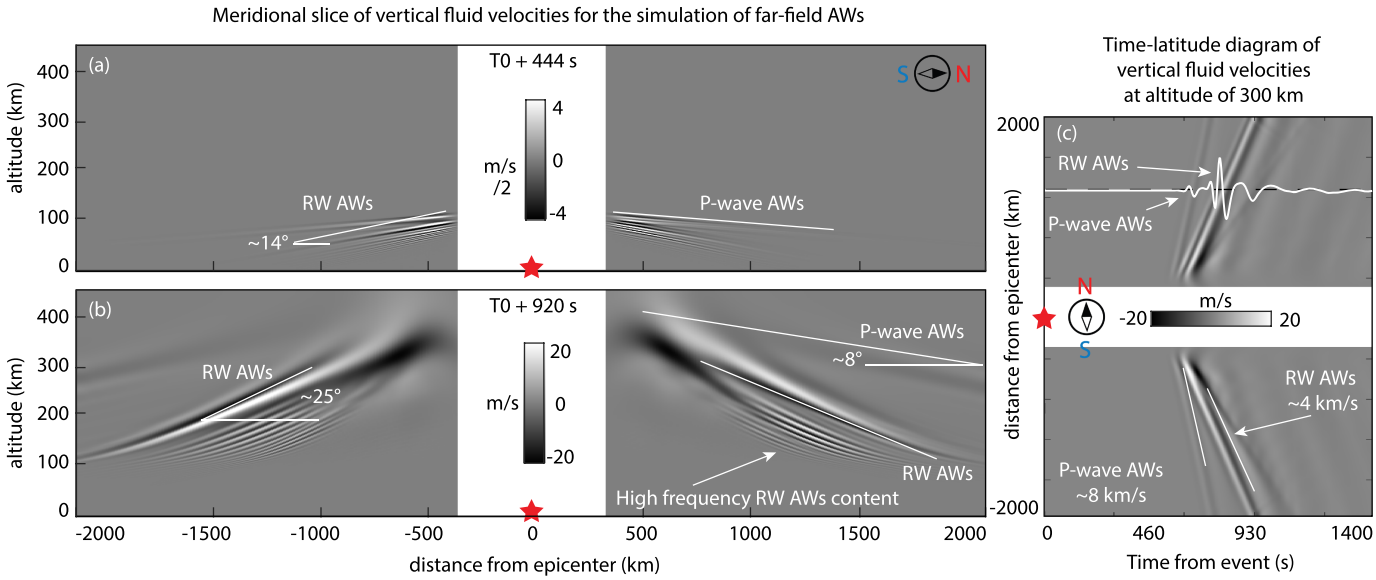

Figure 13. (a,b) Vertical fluid velocities from Simulation (3) for two time epochs. (c) Time-latitude diagram of vertical fluid velocities.

phases from displacements (uplift or subsidence) is not presented here, as was discussed earlier. However, in order to demonstrate the importance of nonlinear effects on AW propagation, we decreased the amplitudes of surface velocities by a factor 100 and reran Simulation (2) with other parameters left unchanged. The results are presented on Figures 12d–12f. In this case, in linear regime of AW propagation, the preservation of phase information of leading AWs can be clearly seen: rarefaction initial phase of leading AWs to the north and compression initial phase of leading AWs to the south. This again demonstrates the importance of AW nonlinear effects for strong waves excited at the near-epicentral region and points to the difficulty of the description of surface deformations based on ionospheric data alone such as TEC.

4.3. Atmosphere-Ionosphere Response to AWs at Far Field

Transient surface displacements from seismic wave propagation induce AWs in the atmosphere. These AWs may also drive observable ionospheric perturbations even at distances far from the epicenter, although usually of small amplitudes (Chum et al., 2012; Ducic et al., 2003). Based on Simulation (3) results, we present snapshots of instantaneous vertical fluid velocities for altitude-latitude slice in Figures 13a and 13b. Time-latitude diagram of vertical fluid velocities at constant altitude of 300 km is shown in Figure 13c. To remind, note again that for this simulation we used meridional slice through GCMT epicenter position.

RWs serve as a source of AWs in the atmosphere that propagate upward with sound speed of ~0.34 km/s at ground level and a wavefront almost parallel (~14° elevation angle) to the surface as it can be seen from Figure 13a. At ionospheric height, due to the marked increase of sound speed with background temperature, the elevation angle of RW AWs wavefronts reaches ~25° (Figure 13b). For *P* waves the elevation angle at ground level is only ~3° and reaches ~8° in ionosphere. Simulation results suggest that far from the epicenter the seismic wave-driven AWs propagate in a linear regime. Only long-period RW AWs propagate to ionospheric heights and reach distances of 2,000 km from epicenter. At distances of 750 km from the epicenter and further maximum vertical fluid velocities of RW AWs are ~25 m/s, ~0.02 TECu with vertical integration and ~0.05 TECu with 30° elevation angle of electron density integration. Comparatively high frequency content of RW AWs is also found in the simulation with ~2.7–3.0 km/s apparent (imprinted by their source) horizontal phase velocities and reaching lower thermosphere; however, they almost fully dissipate below 200–250 km; their vertical fluid velocities do not exceed ~1–3 m/s at 250 km altitude. AWs driven by *P* waves are present (prior to the arrival of RW AWs) propagating with imprinted horizontal phase velocities of ~8 km/s that are consistent with their phase velocities at the surface.

Lognonné et al. (1998) demonstrated that the effective coupling of solid modes with atmosphere happens when solid mode eigenfrequencies are close to the frequencies of the atmospheric waveguides, and revealed two most energetic atmospheric modes of 3.7 and 4.3 mHz. Rolland et al.'s (2011) modeling and observations of RW CIDs for the 2008 Wenchuan M_w7.9 and the 2003 Tokachi-oki M_w8.3 earthquakes support this. The

periods of RW CIDs obtained from Simulation (3) of ~4 mHz support these results. The inclusion of high frequency spectrum of RW AWs to our simulation does not result in stronger and observable CIDs at far field. These frequencies are quite higher than frequencies of ionospheric perturbations registered at Andaman arc region (~2.7 mHz, as reported by Reddy & Seemala, 2015), but this could result from Doppler shift effect due to the motion of IPP position (Savastano, 2018). It is important to note that phase velocities of RWs with frequencies 3.7–4.3 mHz are >3.5 km/s in the considered region (Acton et al., 2010); they are much faster than ionospheric disturbances which were related to RWs based on TEC observations by Reddy and Seemala (2015) propagating with ~2.4 km/s.

Technically, the amplitudes of simulated TEC perturbations driven by RW AWs (0.02–0.05 TECu) can be observed, but we failed to find any such CIDs in the available TEC data set. Probably, they were not resolved spatially within the sparse available measurements or were masked by other ionospheric dynamics, for example, variations in electron density due to the EIA. Simulation assumptions, atmospheric and ionospheric ambient states and winds, source, and models setup may also be insufficient for accurate reproduction of RW CIDs. Planned future investigation of seismic waves-atmosphere-ionosphere coupling processes based on idealized simulations with synthetic sources may clarify discrepancies reported here.

One challenge with the investigation of CIDs based on TEC data is associated with the necessity to use low-elevation angle LOS measurements for their detection. Taking into account that plausible geometry for the detection of CIDs is when AWs wavefront and TEC LOS between station and satellite are parallel (due to integration nature of TEC) to each other, practically only low-elevation angle TEC measurements are useful for the detection of RW CIDs (~ <30°). However, these measurements suffer from multipath, numerous cycle slips, noise levels of phase data, and other errors, which affect the accuracy of TEC measurements (Grewal et al., 2007; Komjathy, 1997). In addition, their IPP velocities cannot be considered as negligible. We refer to Savastano (2018) (section 3.4.1.2) who showed the dependence of IPP velocity from elevation angle using modeling and observational results. The velocities of IPP positions are markedly higher for low-elevation angles and can be up to ~0.6 km/s for 10° measurements. Also, the higher altitudes for ionospheric shell layer, the higher velocities of IPP positions. We assume that for the analysis of low-elevation angle measurements, this effect or appropriate biases should be taken into account.

Source of errors for the analysis of RW CIDs (and CIDs in general) using TEC data may be connected with the choice of ionospheric shell height, or effective height, which is usually linked to peak electron density altitude. The effective height choice results in the determination of IPP position (and subsequently apparent CIDs velocities) and absolute vTEC values and may be highly variable at equatorial latitudes where the nonuniformity of plasma distribution due to the EIA and electrojet provide complex small and medium scale electron density gradients. In equatorial region, a single mean average height cannot be considered to be representative for all LOS of TEC measurements and depends on time of day, the location of observation and the vertical ionization distribution at that location (Rama Rao et al., 2006). In previous observation reports for the Nepal earthquake, the effective height was used as 300–350 km. Chen et al. (2017) calculated it as 328 km based on IRI 2012 model for 25 April 2015. However, as it was shown by Niranjan et al. (2007) (or, for a general case, by Komjathy, 1997), the median models like IRI do not reproduce the spatial distribution of ionization during times when the region is subject to EIA. Rama Rao et al. (2006) discussed the applicability of such altitudes for low-elevation angles measurements for the Indian region. They concluded that the IPP altitude of 350 km may be taken as valid for the Indian peninsula only in cases of TEC elevation angles greater than 50°. Based on monthly mean diurnal variations of h_mF_2 from ionosondes data they showed that at local noon the peak density height can reach altitudes of ~400–500 km. This suggests that for the Indian region, where the RW CIDs were detected, the IPP height, due to EIA effects could be higher than 300–350 km. It also should be noted that far-field CIDs are registered at the proximity of geomagnetic equator, which could markedly affect their apparent propagation direction, velocities and amplitudes retrieved from TEC measurements. At the same time, the choice of IPP position as electron density peak to study ionospheric perturbation is not fully justified because the dominant ion-neutral collisional moment transfer starts at much lower altitudes than the effective height and it plays a main role in plasma disturbances. Thus, for the Nepal earthquake, which happened during local noon, the behavior of plasma could be affected by the presence of the EIA.

In summary, based on the analysis of simulation results of far-field ionospheric perturbations for the Nepal 2015 earthquake we found the following: (1) In marked contrast to those at near-field, AWs driven by seismic

waves at far-field propagate mostly in the linear regime; (2) ionospheric CIDs driven by RWs have similar apparent horizontal phase velocities as RWs at the surface for appropriate periods; (3) thermoviscous dissipative mechanisms markedly attenuate high-frequency content of RW AWs, and mostly long-period RW AWs (~4 mHz) can reach ionospheric heights; (4) the registration of TEC perturbations from body wave-driven transient surface displacements is unlikely; and (5) according to our simulation, the amplitudes of TEC perturbations driven by RW CIDs could be of 0.02–0.05 TECu, but they were not found in the available data set of TEC observations.

5. Conclusion and Future Works

Here we have presented modeling results of ionospheric responses to atmospheric AGWs driven by surface vertical displacements after the 2015 Nepal M_w7.8 Gorkha earthquake and comparisons with observations. Our primary conclusions are as follows: (1) The incorporation of near-field seismic waves dynamic based on finite fault models provides marked improvement for the simulation of realistic AGWs and CIDs at near-field region; the accuracy of finite fault model plays a crucial role in the simulation of realistic ionospheric response and should be chosen appropriately. (2) TEC data at near-field region can serve as a complementary source of information about surface dynamics, but the recovery of information about faulting mechanisms or surface deformations based on TEC are complicated by the loss of phase information of AWs due to nonlinear effects, as well as magnetic field effects on plasma motion. In addition, it should be noted that such analysis can be complicated by unfavorable geometry of TEC measurements, lack of data, or the complexity of the surface dynamics during the earthquakes. (3) The electron depletion can be observed even after this inland earthquake, in the same manner as for large undersea earthquakes, for example, as discussed by Zettergren et al. (2017). (4) The separation of near-field CIDs and those driven by RWs can be detected already at distances of 250–400 km, but, in general, we assume that this distance varies depending on near-field seismic waves dynamic and fault characteristics. (5) The determination of velocities of CIDs (especially RW CIDs) may be hindered by low density of TEC measurements, impacts of EIA, increased IPP velocities for low elevation angle TEC measurements, and geometry of AWs wavefronts and TEC LOS. We found however that the regime of propagation of RW AWs for the event considered could be fairly linear.

In this study we analyzed atmosphere ionosphere response to the Nepal 2015 Gorkha M_w7.8 earthquake. These results may not be all applicable for other events, but reveal several important aspects of earthquake-atmosphere-ionosphere coupling mechanisms that can relate to similar cases. Deeper understanding of these coupling mechanisms can be achieved through further detailed idealized and realistic modeling case studies. Our next step is to apply the coupled 3-D versions of MAGIC and GEMINI models to investigate full 3-D atmosphere-ionosphere responses to realistic sources. Three-dimensionality is particularly important from the point of detailed comparison of modeled and observed TEC perturbations, along real geometry of LOS for every satellite-station pair. Though the practical realization of such coupling is computationally expensive, it will allow us to consider specific cases where the spatial distribution of generated AGWs and driven CIDs cannot be analyzed fully in 2-D or with symmetric sources (such as coupling of 2-D axisymmetric MAGIC and 3-D GEMINI or 3-D MAGIC and 2-D GEMINI).

Acknowledgments
This research was supported by NASA Grants NNX14AQ39G, 80NSSC18K1037 to ERAU and NNH15ZDA001N-ESI via subcontract from JPL. Models used in this study were developed under support from NSF CAREER Grants AGS-1255181 and AGS-1151746. SPECFEM3D-Globe codes are available through this site (https://geodynamics.org/cig/software/specfem3d_globe/). To enable quantitative comparisons and ensure reproducibility, model outputs and detailed movies of the simulations generated for this study are archived at the Embry-Riddle Aeronautical University Library Scholarly Commons, which can be found here (https://commons.erau.edu/dm-2015-nepal-gorkha-earthquake/). Portions of this work were performed at the JPL, California Institute of Technology, under a contract with NASA. The authors gratefully acknowledge the use of the ERAU Vega High-Performance Computing Cluster and the assistance of Scott Hicks. Authors thank Indian Seismic and GNSS Network (ISGN) for making GPS data from the Indian region available for this research. We also thank H. Yue for the discussion and suggestions related to the use of kinematic slip model. Line of Sight Deformation from ALOS-2 Interferometry reported in Lindsey et al. (GRL, 2015) was calculated based on the ALOS-2 satellite L-band InSAR data provided by the Japanese Space Agency (JAXA). Surface displacements from GPS data were calculated using services provided by Natural REsources Canada (https://webapp.geod.nrcan.gc.ca/geod/tools-outils/ppp.php). Broaband seismometers, high-rate GPS and strong motion data were received from UNAVCO and IRIS services http://ds.iris.edu/ds/, and USGS Strong Motion Center https://strongmotioncenter.org/, respectively. We thank J. A. Guerrero for providing software for the investigation of the dependence of IPP position velocity versus elevation angle and thank R. Sabatini, C.J. Heale, B. Piñeyro, and G. Savastano, as well two reviewers, for useful comments and suggestions related to this manuscript.

References

Acton, C. E., Priestley, K., Gaur, V. K., & Rai, S. S. (2010). Group velocity tomography of the Indo-Eurasian collision zone. *Journal of Geophysical Research*, *115*, B12335. https://doi.org/10.1029/2009JB007021

Adhikari, L. B., Gautam, U. P., Koirala, B. P., Bhattarai, M., Kandel, T., Gupta, R. M., et al. (2015). The aftershock sequence of the 2015 April 25 GorkhaNepal earthquake. *Geophysical Journal International*, *203*(3), 2119–2124. https://doi.org/10.1093/gji/ggv412

Astafyeva, E., Heki, K., Kiryushkin, V., Afraimovich, E., & Shalimov, S. (2009). Two-mode long-distance propagation of coseismic ionosphere disturbances. *Journal of Geophysical Research*, *114*, A10307. https://doi.org/10.1029/2008JA013853

Astafyeva, E., Shalimov, S., Olshanskaya, E., & Lognonné, P. (2013). Ionospheric response to earthquakes of different magnitudes: Larger quakes perturb the ionosphere stronger and longer. *Geophysical Research Letters*, *40*, 1675–1681. https://doi.org/10.1002/grl.50398

Azeem, I., Yue, J., Hoffmann, L., Miller, S. D., Straka, W. C., & Crowley, G. (2015). Multisensor profiling of a concentric gravity wave event propagating from the troposphere to the ionosphere. *Geophysical Research Letters*, *42*, 7874–7880. https://doi.org/10.1002/2015GL065903

Bale, D., LeVeque, R. J., Mitran, S., & Rossmanith, J. A. (2002). A wave propagation method for conservation laws and balance laws with spatially varying flux functions. *SIAM Journal on Scientific Computing*, *24*, 955–978. https://doi.org/10.1137/S10648275013973 8X

Bassin, C., Laske, G., & Masters, G. (2000). The current limits of resolution for surface wave tomography in North America. *Eos, Transactions American Geophysical Union*, *81*(F897), 7874–7880.

Bergmann, P. G. (1946). The wave equation in a medium with a variable index of refraction. *The Journal of the Acoustical Society of America*, *17*(4), 329–333. https://doi.org/10.1121/1.1916333

Bilham, R., Gaur, V. K., & Molnar, P. (2001). Himalayan seismic hazard. *Science*, *293*(5534), 1442–1444. https://doi.org/10.1126/science.1062584

Catherine, J. K., Maheshwari, D. U., Gahalaut, V. K., Roy, P. N. S., Khan, P. K., & Puviarasan, N. (2017). Ionospheric disturbances triggered by the 25 April, 2015 M7.8 Gorkha earthquake, Nepal: Constraints from GPS TEC measurements. *Journal of Asian Earth Sciences*, *133*, 80–88. https://doi.org/10.1016/j.jseaes.2016.07.014

Chen, P., Yao, Y., & Yao, W. (2017). On the coseismic ionospheric disturbances after the Nepal M_w7.8 earthquake on April 25, 2015 using GNSS observations. *Advances in Space Research*, *59*(1), 103–113. https://doi.org/10.1016/j.asr.2016.09.021

Chou, M. Y., Lin, C. C. H., Yue, J., Tsai, H. F., Sun, Y. Y., Liu, J. Y., & Chen, C. H. (2017). Concentric traveling ionosphere disturbances triggered by Super Typhoon Meranti (2016). *Geophysical Research Letters*, *44*, 1219–1226. https://doi.org/10.1002/2016GL072205

Chum, J., Cabrera, M. A., Mona, Z., Fagre, M., Bae, J., & Fier, J. (2016). Nonlinear acoustic waves in the viscous thermosphere and ionosphere above earthquake. *Journal of Geophysical Research: Space Physics*, *121*, 12,126–12,137. https://doi.org/10.1002/2016JA023450

Chum, J., Hruska, F., Zednik, J., & Lastovicka, J. (2012). Ionospheric disturbances (infrasound waves) over the Czech Republic excited by the 2011 Tohoku earthquake. *Journal of Geophysical Research*, *117*, A08319. https://doi.org/10.1029/2012JA017767

Clawpack Development Team (2002). Clawpack software. Retrieved from http://www.clawpack.org(Version4.2)

Coïsson, P., Lognonnè, P., Walwer, D., & Rolland, L. M. (2015). First tsunami gravity wave detection in ionospheric radio occultation data. *Earth and Space Science*, *2*(5), 125–133. https://doi.org/10.1002/2014EA000054

Crowell, B. W., Bock, Y., & Melgar, D. (2012). Real-time inversion of GPS data for finite fault modeling and rapid hazard assessment. *Geophysical Research Letters*, *39*, L09305. https://doi.org/10.1029/2012GL051318

Drob, D. P., Emmert, J. T., Meriwether, J. W., Makela, J. J., Doornbos, E., Conde, M., et al. (2015). An update to the Horizontal Wind Model (HWM): The quiet time thermosphere. *Earth and Space Science*, *2*(7), 301–319. https://doi.org/10.1002/2014EA000089

Ducic, V., Artru, J., & Lognonn, P. (2003). Ionospheric remote sensing of the Denali earthquake Rayleigh surface waves. *Geophysical Research Letters*, *30*(18), 1951. https://doi.org/10.1029/2003GL017812

Duputel, Z., Vergne, J., Rivera, L., Wittlinger, G., Farra, V., & Hetnyi, G. (2016). The 2015 Gorkha earthquake: A large event illuminating the Main Himalayan Thrust fault. *Geophysical Research Letters*, *43*, 2517–2525. https://doi.org/10.1002/2016GL068083

Ekström, G., Nettles, M., & Dziewoski, A. M. (2012). The global CMT project 2004-2010: Centroid-moment tensors for 13,017 earthquakes. *Physics of the Earth and Planetary Interiors*, *200–201*, 1–9. https://doi.org/10.1016/j.pepi.2012.04.002

Fan, W., & Shearer, P. M. (2015). Detailed rupture imaging of the 25 April 2015 Nepal earthquake using teleseismic P waves. *Geophysical Research Letters*, *42*, 5744–5752. https://doi.org/10.1002/2015GL064587

Fujii, R., & Sakai, H. (2002). Paleoclimatic changes during the last 2.5 Myr recorded in the Kathmandu Basin, Central Nepal Himalayas. *Journal of Asian Earth Sciences*, *20*(3), 255–266. https://doi.org/10.1016/S1367-9120(01)00048-7

Galetzka, J., Melgar, D., Genrich, J. F., Geng, J., Owen, S., Lindsey, E. O., et al. (2015). Slip pulse and resonance of the Kathmandu Basin during the 2015 Gorkha earthquake, Nepal. *Science*, *349*(6252), 1091–1095. https://doi.org/10.1126/science.aac6383

Galvan, D. A., Komjathy, A., Hickey, M. P., Stephens, P., Snively, J., Tony Song, Y., et al. (2012). Ionospheric signatures of Tohoku-Oki tsunami of March 11, 2011: Model comparisons near the epicenter. *Radio Science*, *47*, RS4003. https://doi.org/10.1029/2012RS005023

Garcia, R. F., Bruinsma, S., Lognonn, P., Doornbos, E., & Cachoux, F. (2013). GOCE: The first seismometer in orbit around the Earth. *Geophysical Research Letters*, *40*, 1015–1020. https://doi.org/10.1002/grl.50205

Grewal, M. S., Weill, L. R., & Andrews, A. P. (2007). *Global Positioning Systems, inertial navigation, and integration*. New York, NY, USA: Wiley-Interscience.

Heale, C. J., Snively, J. B., Hickey, M. P., & Ali, C. J. (2014). Thermospheric dissipation of upward propagating gravity wave packets. *Journal of Geophysical Research: Space Physics*, *119*, 3857–3872. https://doi.org/10.1002/2013JA019387

Hickey, M. P., Schubert, G., & Walterscheid, R. L. (2009). Propagation of tsunami driven gravity waves into the thermosphere and ionosphere. *Journal of Geophysical Research*, *114*, A08304. https://doi.org/10.1029/2009JA014105

Hines, C. O. (1960). Internal atmospheric gravity waves at ionospheric heights. *Canadian Journal of Physics*, *38*(11), 1441–1481. https://doi.org/10.1139/p60-150

Huba, J. D., Joyce, G., & Fedder, J. A. (2000). Sami2 is another model of the ionosphere (SAMI2): A new low-latitude ionosphere model. *Journal of Geophysical Research*, *105*(A10), 23,035–23,053. https://doi.org/10.1029/2000JA000035

Igel, H. (2017). *Computational seismology, A practical introduction*. Oxford: Oxford University Press.

Jin, S., Occhipinti, G., & Jin, R. (2015). GNSS ionospheric seismology: Recent observation evidences and characteristics. *Earth-Science Reviews*, *147*, 54–64. https://doi.org/10.1016/j.earscirev.2015.05.003

Kargel, J. S., Leonard, G. J., Shugar, D. H., Haritashya, U. K., Bevington, A., Fielding, E. J., et al. (2016). Geomorphic and geologic controls of geohazards induced by Nepal's 2015 Gorkha earthquake. *Science*, *351*(6269). https://doi.org/10.1126/science.aac8353

Kobayashi, T., Morishita, Y., & Yarai, H. (2015). Detailed crustal deformation and fault rupture of the 2015 Gorkha earthquake, Nepal, revealed from ScanSAR-based interferograms of ALOS-2. *Earth Planets Space*, *67*(1), 201. https://doi.org/10.1186/s40623-015-0359-z

Komatitsch, D., Michéa, D., & Erlebacher, G. (2009). Porting a high-order finite-element earthquake modeling application to NVIDIA graphics cards using CUDA. *Journal of Parallel and Distributed Computing*, *69*(5), 451–460. https://doi.org/10.1016/j.jpdc.2009.01.006

Komatitsch, D., & Tromp, J. (2002a). Spectral-element simulations of global seismic wave propagation. Validation. *Geophysical Journal International*, *149*(2), 390–412. https://doi.org/10.1046/j.1365-246X.2002.01653.x

Komatitsch, D., & Tromp, J. (2002b). Spectral-element simulations of global seismic wave propagation. Three-dimensional models, oceans, rotation and self-gravitation. *Geophysical Journal International*, *150*(1), 303–318. https://doi.org/10.1046/j.1365-246X.2002.01716.x

Komjathy, A. (1997). Global ionospheric total electron content mapping using the Global Positioning System (Ph.D. dissertation), Department of Geodesy and Geomatics Engineering Technical Report No. 188, University of New Brunswick, Fredericton, New Brunswick, Canada.

Komjathy, A., Yang, Y.-M., Meng, X., Verkhoglyadova, O., Mannucci, A. J., & Langley, R. B. (2016). Review and perspectives: Understanding natural hazards-generated ionospheric perturbations using GPS measurements and coupled modeling. *Radio Science*, *51*, 951–961. https://doi.org/10.1002/2015RS005910

Kustowski, B., Ekström, G., & Dziewoski, A. M. (2008). Anisotropic shear-wave velocity structure of the Earth's mantle: A global model. *Journal of Geophysical Research*, *113*, B06306. https://doi.org/10.1029/2007JB005169

Langseth, J. O., & LeVeque, R. J. (2000). A wave propagation method for three dimensional hyperbolic conservation laws. *Journal of Computational Physics*, *165*(1), 126–166. https://doi.org/10.1006/jcph.2000.6606

LeVeque, R. J. (2002). *Finite volume methods for hyperbolic problems*. Cambridge: Cambridge University Press.

Lin, C. C. H., Shen, M.-H., Chou, M.-Y., Chen, C.-H., Yue, J., Chen, P.-C., & Matsumura, M. (2017). Concentric traveling ionospheric disturbances triggered by the launch of a SpaceX Falcon 9 rocket. *Geophysical Research Letters*, *44*, 7578–7586. https://doi.org/10.1002/2017GL074192

Lindsey, E. O., Natsuaki, R., Xu, X., Shimada, M., Hashimoto, M., Melgar, D., & Sandwell, D. T. (2015). Line-of-sight displacement from ALOS-2 interferometry: M_w 7.8 Gorkha earthquake and M_w 7.3 aftershock. *Geophysical Research Letters*, *42*, 6655–6661. https://doi.org/10.1002/2015GL065385

Liu, H., Ding, F., Zhao, B., Li, J., Hu, L., Wan, W., & Ning, B. (2017). Ionospheric response following the M_w 7.8 Gorkha earthquake on 25 April 2015. *Journal of Geophysical Research*, *122*, 6495–6507. https://doi.org/10.1002/2016JA023079

Lognonné, P., Clévédé, E., & Kanamori, H. (1998). Computation of seismograms and atmospheric oscillations by normal-mode summation for a spherical earth model with realistic atmosphere. *Geophysical Journal International*, *135*(2), 388–406. https://doi.org/10.1046/j.1365-246X.1998.00665.x

Masashi, K., Tatsuya, K., Yoshiaki, O., Atsushi, T., Yuko, S., Shoho, T., & Jann-Yenq, L. (2015). Does an ionospheric hole appear after an inland earthquake? *Journal of Geophysical Research*, *120*, 9998–10,005. https://doi.org/10.1002/2015JA021476

Matsumura, M., Saito, A., Iyemori, T., Shinagawa, H., Tsugawa, T., Otsuka, Y., et al. (2011). Numerical simulations of atmospheric waves excited by the 2011 off the Pacific coast of Tohoku Earthquake. *Earth Planets Space*, *63*(7), 68. https://doi.org/10.5047/eps.2011.07.015

Meng, X., Verkhoglyadova, O. P., Komjathy, A., Savastano, G., & Mannucci, A. J. (2018). Physics-based modeling of earthquake-induced ionospheric disturbances. *Journal of Geophysical Research: Space Physics*, *123*, 8021–8038. https://doi.org/10.1029/2018JA025253

Mikhailov, A. A., & Martynov, V. N. (2017). Numerical modeling of the infrasonic and seismic waves propagation in the earth-atmosphere model with a curvilinear interface. *AIP Conference Proceedings*, *1907*(1), 30036. https://doi.org/10.1063/1.5012658

Nakashima, Y., & Heki, K. (2014). Ionospheric hole made by the 2012 North Korean rocket observed with a dense GNSS array in Japan. *Radio Science*, *49*(7), 497–505. https://doi.org/10.1002/2014RS005413

Niranjan, K., Srivani, B., Gopikrishna, S., & Rama Rao, P. S. V. (2007). Spatial distribution of ionization in the equatorial and low-latitude ionosphere of the Indian sector and its effect on the pierce point altitude for GPS applications during low solar activity periods. *Journal of Geophysical Research*, *112*, A05304. https://doi.org/10.1029/2006JA011989

Nishioka, M., Tsugawa, T., Kubota, M., & Ishii, M. (2013). Concentric waves and short-period oscillations observed in the ionosphere after the 2013 Moore EF5 tornado. *Geophysical Research Letters*, *40*, 5581–5586. https://doi.org/10.1002/2013GL057963

Occhipinti, G., Coïsson, P., Makela, J. J., Allgeyer, S., Kherani, A., Hebert, H., & Lognonné, P. (2011). Three-dimensional numerical modeling of tsunami-related internal gravity waves in the Hawaiian atmosphere. *Earth Planets Space*, *63*(7), 61. https://doi.org/10.5047/eps.2011.06.051

Occhipinti, G., Lognonné, P., Kherani, E. Alam, & Hebert, H. (2006). Three-dimensional waveform modeling of ionospheric signature induced by the 2004 Sumatra tsunami. *Geophysical Research Letters*, *33*, L20104. https://doi.org/10.1029/2006GL026865

Occhipinti, G., Rolland, L., Lognonné, P., & Watada, S. (2013). From Sumatra 2004 to Tohoku-Oki 2011: The systematic GPS detection of the ionospheric signature induced by tsunamigenic earthquakes. *Journal of Geophysical Research*, *118*, 3626–3636. https://doi.org/10.1002/jgra.50322

Otsuka, Y., Kotake, N., Tsugawa, T., Shiokawa, K., Ogawa, T., Effendy, et al. (2006). GPS detection of total electron content variations over Indonesia and Thailand following the 26 December 2004 earthquake. *Earth Planets Space*, *58*(2), 159–165. https://doi.org/10.1186/BF03353373

Parkinson, B., Spilker, J., Axelrad, P., & Enge, P. (1995). Global Positioning System: Theory and applications.

Picone, J. M., Hedin, A. E., Drob, D. P., & Aikin, A. C. (2002). NRLMSISE-00 empirical model of the atmosphere: Statistical comparisons and scientific issues. *Journal of Geophysical Research*, *107*(A12), 1468. https://doi.org/10.1029/2002JA009430

Pilger, C., Schmidt, C., Streicher, F., Wüst, S., & Bittner, M. (2013). Airglow observations of orographic, volcanic and meteorological infrasound signatures. *Journal of Atmospheric and Solar-Terrestrial Physics*, *104*, 55–66. https://doi.org/10.1016/j.jastp.2013.08.008

Qin, W., & Yao, H. (2017). Characteristics of subevents and three-stage rupture processes of the 2015 M_w 7.8 Gorkha Nepal earthquake from multiple-array back projection. *Journal of Asian Earth Sciences*, *133*, 72–79. https://doi.org/10.1016/j.jseaes.2016.11.012

Rama Rao, P. V. S., Niranjan, K., Prasad, D. S. V. V. D., Gopi Krishna, S., & Uma, G. (2006). On the validity of the ionospheric pierce point (IPP) altitude of 350 km in the Indian equatorial and low-latitude sector. *Annales Geophysicae*, *24*(8), 2159–2168. https://doi.org/10.5194/angeo-24-2159-2006

Reddy, C. D., & Seemala, G. K. (2015). Two-mode ionospheric response and Rayleigh wave group velocity distribution reckoned from GPS measurement following M_w 7.8 Nepal earthquake on 25 April 2015. *Journal of Geophysical Research*, *120*, 7049–7059. https://doi.org/10.1002/2015JA021502

Ritzwoller, M. H., & Levshin, A. L. (1998). Eurasian surface wave tomography: Group velocities. *Journal of Geophysical Research*, *103*(B3), 4839–4878. https://doi.org/10.1029/97JB02622

Rolland, L. M., Lognonné, P., & Munekane, H. (2011). Detection and modeling of Rayleigh wave induced patterns in the ionosphere. *Journal of Geophysical Research*, *116*, A05320. https://doi.org/10.1029/2010JA016060

Sabatini, R., Bailly, C., Marsden, O., & Gainville, O. (2016). Characterization of absorption and non-linear effects in infrasound propagation using an augmented Burgers equation. *Geophysical Journal International*, *207*(3), 1432–1445. https://doi.org/10.1093/gji/ggw350

Sabatini, R., Marsden, O., Bailly, C., & Gainville, O. (2019). Three-dimensional direct numerical simulation of infrasound propagation in the Earth's atmosphere. *Journal of Fluid Mechanics*, *859*, 754–789. https://doi.org/10.1017/jfm.2018.816

Saito, A., Tsugawa, T., Otsuka, Y., Nishioka, M., Iyemori, T., Matsumura, M., et al. (2011). Acoustic resonance and plasma depletion detected by GPS total electron content observation after the 2011 off the Pacific coast of Tohoku Earthquake. *Earth, Planets and Space*, *63*(7), 64. https://doi.org/10.5047/eps.2011.06.034

Savastano, G. (2018). New applications and challenges of GNSS variometric approach (Doctoral dissertation), The University of Rome La Sapienza. http://hdl.handle.net/11573/1077041

Schunk, R., & Nagy, A. (2009). *Ionospheres: Physics, plasma physics, and chemistry* (2nd ed.)., Cambridge Atmospheric and Space Science Series: Cambridge University Press. https://doi.org/10.1017/CBO9780511635342

Snively, J. B. (2013). Mesospheric hydroxyl airglow signatures of acoustic and gravity waves generated by transient tropospheric forcing. *Geophysical Research Letters*, *40*, 4533–4537. https://doi.org/10.1002/grl.50886

Sunil, A. S., Bagiya, M. S., Catherine, J., Rolland, L., Sharma, N., Sunil, P. S., & Ramesh, D. S. (2017). Dependence of near field co-seismic ionospheric perturbations on surface deformations: A case study based on the April, 25 2015 Gorkha Nepal earthquake. *Advances in Space Research*, *59*(5), 1200–1208. https://doi.org/10.1016/j.asr.2016.11.041

Takai, N., Shigefuji, M., Rajaure, S., Bijukchhen, S., Ichiyanagi, M., Dhital, M. R., & Sasatani, T. (2016). Strong ground motion in the Kathmandu Valley during the 2015 Gorkha, Nepal, earthquake. *Earth Planets Space*, *68*(1), 10. https://doi.org/10.1186/s40623-016-0383-7

Tulasi Ram, S., Sunil, P. S., Ravi, K. M., Su, S.-Y., Tsai, L. C., & Liu, C. H. (2017). Coseismic traveling ionospheric disturbances during the M_w 7.8 Gorkha, Nepal, Earthquake on 25 April 2015 from ground and saceborne observations. *Journal of Geophysical Research: Space Physics*, *122*, 10,669–10,685. https://doi.org/10.1002/2017JA023860

Wang, K., & Fialko, Y. (2015). Slip model of the 2015 M_w 7.8 Gorkha (Nepal) earthquake from inversions of ALOS-2 and GPS data. *Geophysical Research Letters*, *42*, 7452–7458. https://doi.org/10.1002/2015GL065201

Wei, S., Chen, M., Wang, X., Graves, R., Lindsey, E., Wang, T., et al. (2018). The 2015 Gorkha (Nepal) earthquake sequence: I. Source modeling and deterministic 3D ground shaking. *Tectonophysics*, *722*, 447–461. https://doi.org/10.1016/j.tecto.2017.11.024

Whitham, G. B. (1974). *Linear and nonlinear waves*. New York: A Wiley-Interscience publication.

Yue, H., Simons, M., Duputel, Z., Jiang, J., Fielding, E., Liang, C., et al. (2016). Depth varying rupture properties during the 2015 M_w 7.8 Gorkha (Nepal) earthquake. *Tectonophysics*, *714-715*, 44–54. https://doi.org/10.1016/j.tecto.2016.07.005

Zettergren, M. D., & Semeter, J. (2012). Ionospheric plasma transport and loss in auroral downward current regions. *Journal of Geophysical Research*, *117*, A06306. https://doi.org/10.1029/2012JA017637

Zettergren, M. D., & Snively, J. (2013). Ionospheric signatures of acoustic waves generated by transient tropospheric forcing. *Geophysical Research Letters*, *40*, 5345–5349. https://doi.org/10.1002/2013GL058018

Zettergren, M. D., & Snively, J. B. (2015). Ionospheric response to infrasonic-acoustic waves generated by natural hazard events. *Journal of Geophysical Research*, *120*, 8002–8024. https://doi.org/10.1002/2015JA021116

Zettergren, M. D., & Snively, J. B. (2019). Latitude and longitude dependence of ionospheric TEC and magnetic perturbations from infrasonic-acoustic waves generated by strong seismic events. *Geophysical Research Letters*, *46*, 1132–1140. https://doi.org/10.1029/2018GL081569

Zettergren, M. D., Snively, J. B., Komjathy, A., & Verkhoglyadova, O. P. (2017). Nonlinear ionospheric responses to large-amplitude infrasonic-acoustic waves generated by undersea earthquakes. *Journal of Geophysical Research: Space Physics*, *122*, 2272–2291. https://doi.org/10.1002/2016JA023159

Zhang, L., Li, J., Liao, W., & Wang, Q. (2016). Source rupture process of the 2015 Gorkha, Nepal M_w7.9 earthquake and its tectonic implications. *Geodesy and Geodynamics*, *7*(2), 124–131. https://doi.org/10.1016/j.geog.2016.03.001

Zhou, Y., Yang, J., Zhu, F., Su, F., Hu, L., & Zhai, W. (2017). Ionospheric disturbances associated with the 2015 M7.8 Nepal earthquake. *Geodesy and Geodynamics*, *8*(4), 221–228. https://doi.org/10.1016/j.geog.2017.04.004